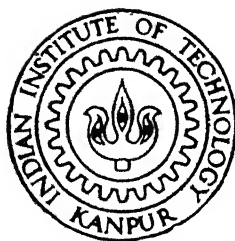


# X-RAY, SPECTROSCOPIC AND THERMAL GAS EFFUSION STUDIES OF ELECTROCHEMICALLY FORMED POROUS SILICON

by

**MANOJ KUMAR SINGH**



TH  
MSP/1997/M  
Si 64x

**MATERIALS SCIENCE PROGRAMME**

**INDIAN INSTITUTE OF TECHNOLOGY KANPUR**

**OCTOBER. 1997**

# X-RAY, SPECTROSCOPIC AND THERMAL GAS EFFUSION STUDIES OF ELECTROCHEMICALLY FORMED POROUS SILICON

A Thesis Submitted in  
Partial Fulfilment of the Requirements  
for the Degree of  
MASTER OF TECHNOLOGY

*by*  
*Manoj Kumar Singh*

to the  
Materials Science Programme  
Indian Institute of Technology, Kanpur  
October, 1997

5 DEC 1997

CENTRAL LIBRARY  
I. I. T., KANPUR

---

Acc. No. A 124452



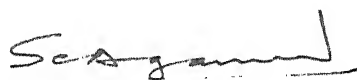
A124452

M. S. D. 1987 M. S. N. 1987

**TO MY BELOVED  
FAMILY**

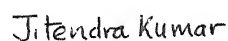
## CERTIFICATE

This is to certify that the work contained in the thesis entitled "**X-ray, spectroscopic and thermal gas effusion studies of electrochemically formed porous silicon**", by Manoj Kumar Singh, has been carried out under our supervision and that the same has not been submitted elsewhere for a degree.



---

S. C. Agarwal  
Professor  
Department of Physics  
Indian Institute of Technology  
Kanpur 208 016 (U.P.)



---

Jitendra Kumar  
Professor  
Materials Science Programme  
Indian Institute of Technology  
Kanpur 208 016 (U.P.)

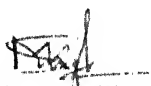
October, 1997

## ACKNOWLEDGEMENTS

I express my gratitude to my thesis supervisors Dr S. C. Agarawal and Dr Jitendra Kumar for being extremely cooperative and their understanding throughout my M. Tech thesis. They have taught me many things and helped me in many ways in both academic and other matters. It has been thrilling to work with them.

I am indebted to Dr Prem Chand for his help and interaction in EPR studies, Dr Asima Pradhan for Raman measurements and Central Drug Research Institute, Lucknow for extending FTIR facility. My thanks are due to my labmates Alok, Dr Pratima Agarwal for their invaluable help. I am thankful to Gurvinder, Pragya, Prashant and Manoj for their wonderful company and co-operation in all moments. I am also thankful to Mr Dinesh Kanaujia for help in EPR and Mr H K Pandey to type my manuscript very nicely.

I am grateful to my friends, Ajeet, Rajneesh, Suresh, Pankaj and Gaurav who make my stay at IIT Kanpur memorable.



***Manoj Kumar Singh***

## Contents

Abstract	i
Acknowledgements	ii
List of Figures	iii
List of Tables	iv
<b>1. Introduction</b>	<b>1</b>
1.1 Porous silicon	1
1.2 Objective of present work	5
<b>2. Experimental Details</b>	<b>6</b>
2.1 Formation of porous silicon	6
2.1.1 Substrate preperation	6
2.1.2 Electrochemical etching	8
2.2 Characterization methods	11
2.2.1 Raman scattering	11
2.2.2 X-ray diffraction	14
2.2.3 EPR spectroscopy	14
2.2.4 Thermal gas effusion	15
2.2.5 FTIR spectroscopy	19
2.3 Peakfit analysis	19
<b>3. Results and Discussion</b>	<b>21</b>
3.1 Raman spectroscopy	21
3.2 X-ray diffraction	28
3.3 Electron paramagnetic resonance (EPR) spectroscopy	31
3.4 Thermal gas effusion	36
3.5 (FTIR) studies	47
<b>4. Conclusions</b>	<b>56</b>
<b>References</b>	<b>58</b>

## List of Figures

<u>No.</u>	<u>Caption</u>	<u>Pages</u>
1.1	Schematic diagram of a semiconductor quantum well.	4
2.1	Schematic diagram of annealing set-up.	7
2.2	Flow diagram of a substrate preparation steps.	9
2.3	A set-up for electrochemical cell etching of silicon.	10
2.4	Origin of Raman spectra.	13
2.5	Schematic diagram of thermal effusion set-up.	16
2.6	A quadrupole mass spectrometer.	18
2.7	Scheme of a fourier transform spectrometer.	20
3.1	Raman spectra of a standard c-Si.	22
3.2	Raman spectra of porous silicon PSL2 from two regions dominating : (a) solid structure and (b) crack.(or pores).	23
3.3	Raman spectra of porous silicon PSL6 from two regions dominating : (a) solid structure and (b) crack.(or pores).	24
3.4	Raman spectra of porous silicon PSL13 from two regions dominating : (a) solid structure and (b) crack.(or pores).	25
3.5	The relationship between the redshift observed in PS with respect to that of c-Si and the FWHM of Raman resonance peak.	27
3.6	X-ray diffractograms of PSL2 (a) in virgin state and after annealing upto (b) 450 <sup>0</sup> C, and (c) upto 650 <sup>0</sup> C.	29
3.7	X-ray diffractograms of PSL6 (a) in virgin state and after annealing upto (b) 250 <sup>0</sup> C, and (c) upto 450 <sup>0</sup> C.	30
3.8	EPR spectrum of PSL2 in virgin state and the standard DPPH sample.	34
3.9	EPR spectrum of PSL2 after annealing upto 450 <sup>0</sup> C and the standard DPPH sample.	35



3.10	The variation of 'g'-values as a function of annealing temperature in porous silicon.	37
3.11	A graph between EPR peak width and annealing temperature in porous silicon.	38
3.12	A graph between spin numbers and annealing temperature in porous silicon.	39
3.13	Thermal gas effusion spectrum of PSL1 as a function of temperature: For (a) H, H <sub>2</sub> , SiH, SiH <sub>2</sub> , SiH <sub>3</sub> , SiF and SiFH and (b) H, H <sub>2</sub> , O, O <sub>2</sub> species.	40
3.14	Thermal gas effusion spectrum of PSL11 as a function of temperature.	41
3.15	Hydrogen gas evolution characteristic of PSL1 as derived from "peak fit" analysis of experimental data.	43
3.16	SiH gas evolution characteristic of (a) PSL1 and (b) PSL11 as derived from "peak fit" analysis of experimental data.	44
3.17	SiH <sub>2</sub> gas evolution characteristic of (a) PSL1 and (b) PSL11 as derived from "peak fit" analysis of experimental data.	45
3.18	SiH <sub>3</sub> gas evolution characteristic of (a) PSL1 and (b) PSL11 as derived from "peak fit" analysis of experimental data.	46
3.19	FTIR spectra of PSL2 (a) in virgin state and (b) after annealing upto 450 <sup>0</sup> C.	48
3.20	FTIR spectra of PSL6 (a) in virgin state and (b) after annealing upto 250 <sup>0</sup> C.	49
3.21	FTIR spectra of PSL13 in virgin state.	50

## List of Tables

No.	<u>Caption</u>	<u>Pages</u>
2.1	Preparation conditions of porous silicon (PS) samples	8
2.2	The ions traced in thermal effusion of porous silicon.	17
3.1	Peak positions and their FWHM ranges for various Raman spectra shown in Figs. 3.1-3.4 of porous silicon.	26
3.2	X-ray line broadening data of porous silicon with average size of crystallites.	31
3.3	Comparison of EPR g-values for spin centres consisting of an unpaired electron at a Si dangling bond.	32
3.4	Effect of annealing on EPR signal and related parameters in porous silicon.	36
3.5	Thermal gas effusion data of porous silicon in the process of annealing at the rate of $9.6^{\circ}\text{C}/\text{min}$ under vacuum $\sim 10^{-6}$ torr.	47
3.6	Summary of the IR data available in the literature for vibrations mode and species relevant to porous silicon [57-66].	51
3.7	FTIR spectrum data of PSL2 giving peak position, percentage absorption at peak maxima and corresponding modes/species.	52
3.8	FTIR spectrum data of PSL6 giving peak position, percentage absorption at peak maxima and corresponding modes/species.	53
3.9	FTIR spectrum data of PSL13 giving peak position, percentage absorption at peak maxima and corresponding modes/species.	54

### 1. Introduction

Silicon is at the heart of the microelectronics revolution. Its dominance is intimately tied to the (i) superior materials and processing properties, and (ii) development of vast base of technology [1]. Silicon, however, exhibits an indirect band gap and is a poor light emitter. For this reason, it has not found much acceptance in optical applications [1]. The importance of developing a technology that allows integration of optical and electronic devices on a silicon wafer has long been recognized [1]. Such an advance is likely to have a significant impact on display, communications, computer and a host of related areas. Today, light-emitting devices are fabricated almost exclusively from semiconductors such as gallium arsenide (GaAs), indium phosphide (InP), etc. which display a direct-band gap and relatively higher optical efficiency. Alternatively, efforts are made either to improve the efficiency of silicon itself or to develop silicon-compatible material with high optical efficiency. Considerable research has been carried out in this direction using techniques that range from the engineering of superlattices and quantum wells (composed of silicon, germanium and carbon) to the doping of silicon with optically efficient rare earths, such as erbium [1]. Nevertheless, the progress made is too little to improve the optical efficiency significantly.

In 1990, Canham [2] observed room-temperature photoluminescence in the visible range from the porous silicon (PS) formed on a silicon wafer. This property of porous silicon was of interest for several reasons. Firstly, the emitting light had energy well above the band gap of bulk silicon. Secondly, the energy (or colour) could be tuned throughout the visible spectrum by changing the preparation conditions of porous silicon-an important consideration for display devices involving red, green and blue colours. Finally, the quantum efficiency of PS was found to be  $\sim 10\%$ , i.e., comparable to that of direct-band gap compound semiconductors.

#### 1.1 Porous Silicon

It is simply a network of nanometer-sized silicon crystallites surrounded by voids. It is usually prepared by electrochemical etching/anodization of silicon wafers and characterized by a structure consisting of a large number of micro-(diameter  $< 2\text{nm}$ ), meso-

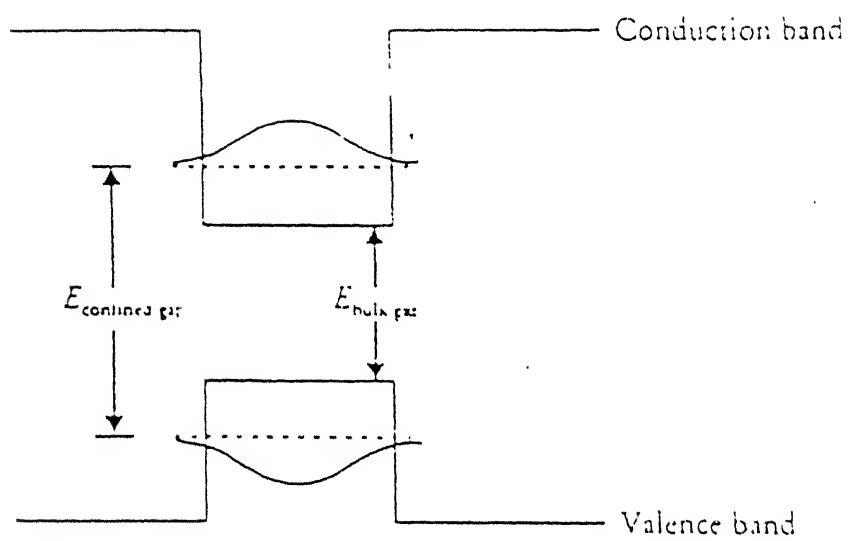
(2 - 50 nm) and macro-( > 50 nm) pores. Although, interest in the light-emitting properties of porous silicon is a rather recent development, it was discovered in 1956 during electropolishing of silicon [3]. A brittle, spongy, thread like structure was obtained exhibiting a variety of pore geometries within an otherwise crystalline material. The morphologies varied from a network of fine interconnected pores to linear and wide pipe-like pores. Also, the pore size and shape were found to depend upon the nature of doping (n- or p- type and concentration), the anodization current density, electrolyte and its concentrations, etc. The properties of PS layers were studied extensively because of their potential use in electronic isolation technologies, such as silicon-on-insulator (SOI) and fully isolated porous silicon (FIPOS).

PS can be prepared by several methods. The most commonly used being the electrochemical etching of crystalline silicon (c-Si) in a dilute solution (~ 25%) of HF and ethanol [1,2]. Other methods include spark erosion [4,5] and light induced etching of c-Si in HF [6,7]. Generally, p- or n- type c-Si wafer is made an anode and etched selectively by passing a constant current in an electrolytic cell containing HF solution. It is indeed necessary to illuminate n-type substrate during the etching process for yielding porous silicon [8]. But, a p-type wafer gives rise to PS even if etching is performed in dark. A variety of PS layers with a host of pore morphologies and controllable thickness can now be prepared. Also, successful attempts have been made to even prepare free - standing films of PS [9]. The discovery of photoluminescence in PS at room temperature in red-yellow region marked the opening of an altogether new field of research because of its technological potential. Consequently, research work focussed around explaining the phenomenon of visible luminescence itself. Bulk crystalline silicon (or c-Si) has a relatively small but indirect energy band-gap (~ 1.12 eV), making interband radiative recombination process inefficient and difficult. At room temperature, c-Si shows a weak photoluminescence (PL) in the IR region at about 1.12 eV with a full width at half maximum (FWHM) varying with excitation conditions, but is typically ~ 0.1 eV [10,11]. In contrast, PS shows a strong PL in the visible region at about 1.4-2.0 eV with a comparatively narrow FWHM; the exact peak position, however, depends upon the preparation conditions and post-etching chemical treatments [2,12-14].

The structural aspects of PS are viewed in terms of its crystallinity which deteriorates with increasing level of porosity and eventually leads to an amorphous phase [15]. Canham [2] attributed the luminescence phenomenon to widening of band gap due to quantum

confinement of electrons/holes in the nanosized columnar structures. This argument was based on simple Heisenberg principle and involved downward and upward shifts of the valence and conduction-band edges, respectively (Fig. 1.1). Further support to the above explanation was provided by Raman spectra of PS, which, invariably contained a low frequency side band corresponding to a shorter coherence length of optical phonons in the direction perpendicular to the pore axis [16]. The transmission electron microscopic studies also reveal the presence of nano-sized crystallites in PS [17]. Moreover, quantum confinement model has successfully explained the visible luminescence phenomenon in various systems containing silicon nanocrystals but produced by techniques other than etching [18-22]. Nevertheless, Brandt et.al. [16] put forward an alternative explanation, now known as Siloxene model. Accordingly, visible luminescence in PS is not an intrinsic property of nanostructures of c-Si, but, results from the compounds (siloxene,  $\text{Si}_6\text{O}_3\text{H}_6$ ; and its derivatives) formed by the chemical reactions of silicon with hydrogen and oxygen. The basis for this proposition lies in a striking resemblance found in the luminescent behaviour (e.g., life-time, intensity, position, shift, etc.) of PS and vibrational properties of Kautsky and Wohler compounds derived from siloxene [16]. For example, (i) etching of PS with an electrolyte containing a mixture of HF, HCl, and ethanol results in a luminescence band centred at 690 nm. This agrees well with the fluorescence observed in siloxene after annealing at 673 K, the larger peak width here is due to rather uncontrolled substitution of hydrogen by OH groups during the treatment, (ii) the red luminescence in PS found after etching in a solution of HF and ethanol has a maximum at 760 nm, which is in quantitative agreement with the fluorescence peak of siloxene after annealing at 673 K. Infra-red (IR) and Raman spectra further corroborated the siloxene model [16]. In yet another model, etching process is believed to form Si-hydride on the large surface area of PS and excitations in them are responsible for the photoluminescence [23,24]. Moreover, the distribution of hydrides determines the peak position while total surface area of PS layers influence the intensity of the PL spectra. The experimental observations that led to this model include red shift and gradual disappearance of PL on annealing at temperatures in the range of 503-663 K, blue shift in PL peaks due to pore widening in PS after chemical etching with HF [23], etc. It can therefore be inferred that photoluminescence (PL) phenomenon in porous silicon is still not fully understood.

Apart from visible PL, electroluminescence (EL) was observed in PS though with disappointingly poor efficiency ( $\sim 0.01\%$ ) [25-27]. This initiated studies on PS with regard



1.1 Schematic diagram of a semiconductor quantum well.

to carrier transport properties too. Also, metal contacts on PS layers are found to act as light emitting diodes [25]. It is worth mentioning here that PS in general has a complex microstructure : quantum wire columnar structure, oxidised (or otherwise passivated) partially connected spheres of silicon with tissue like morphology, amorphous with small embedded Si nanocrystals, etc. Its exact nature, however, varies with the substrate resistivity, porosity level, and thickness.

## 1.2 Objective of present work

Ever since visible PL was discovered in porous silicon [2], enormous studies have been undertaken using different characterization techniques for obtaining complimentary information [28-31]. However, thermal stability aspects and the nature of chemical species present in PS have not been investigated in depth [32]. Since the mode of preparation of PS involves electrochemical bath containing HF and alcohol, many different chemical species are likely to be present. Further, PS has a large surface-to-volume ratio ( $\sim 4 \times 10^8 \text{ m}^2/\text{m}^3$ ) and very high density of dangling bonds at the surface [33]. These dangling bonds may act as traps or non-radiative recombination centres for the photo-generated electron-hole pairs. There exists several reports on optical and transport properties of the PS to suggest that the processes at the surface play a dominant role in determining its behaviour [34-36]. It is important therefore to have a reliable and quantitative method of identifying surface desorbed species in PS for evaluation of its thermal stability. In the present work, an attempt is made to prepare porous silicon by usual electrochemical process and monitor its effusion characteristics on heating in vacuum  $\sim 10^{-6}$  torr by thermally stimulated effusion (TSE) and FTIR spectroscopy. In addition, complimentary techniques consisting of Raman and e.p.r. spectroscopies and X-rays diffraction have been utilized to gather information with regard to microcrystallinity, dangling bonds/spin density, phase identification with orientation disposition and grain size, etc. for arriving at the better insight of the nature of porous silicon.

## Chapter 2

### 2. Experimental details

This chapter contains details of the preparation of porous silicon and characterization techniques used. Sample preparation is a long process and involves several steps, viz., cleaning of silicon wafers, metal deposition for back contact, electrochemical etching under controlled conditions, drying, etc. For characterization of porous silicon, Raman spectroscopy, X-ray diffraction, electron para magnetic resonance (EPR) spectroscopy, thermal gas effusion and fourier transform infrared (FTIR) spectroscopy are employed.

#### 2.1 Formation of porous silicon

##### 2.1.1 Substrate Preparation

The substrate used was a p-type (boron doped) polished c-Si wafer of resistivity  $\rho = 0.5\text{-}10\Omega\text{-cm}$  and orientation  $\langle 100 \rangle$ . It was cleaned chemically in a multistep process. First the wafer was boiled in trichloroethylene (TCE) to degrease and rinsed with ethanol to remove the residue. The wafer was further cleaned in an ultrasonic cleaner using acetone. The oxide layer that usually exists on Si-wafer was removed by etching using a dilute solution (20%) of HF in ethanol for about 30-40 s. It was then rinsed with deionised water. The resulting surface was generally hydrophobic in nature. For back contact, aluminium was evaporated thermally in vacuum ( $\sim 10^{-5}$  torr) and allowed to deposit on the unpolished (or back) surface of c-Si wafer. The evaporation source was a tungsten filament (i.e., a basket) and held underneath and facing the back surface of c-Si. To ensure high quality of aluminium film, evaporation was carried out under vacuum  $\sim 10^{-5}$  torr or better. Due to the oxide surface layer invariably formed during the transfer of c-Si into the vacuum chamber even, there develops a barrier across the silicon-aluminium interface. This makes the contact non-ohmic in nature. To overcome this difficulty, the aluminium coated silicon was annealed at  $\sim 550^{\circ}\text{C}$  for about half an hour. At this temperature, interatomic diffusion occurs at the interface leading to alloy formation. Fig 2.1 shows the schematic diagram of the annealing set-up. It consists of a hollow cylindrical furnace, a quartz tube connected to a pumping system and arrangement of measuring the temperature inside through a thermocouple. Aluminium back coated c-Si wafers were placed inside the



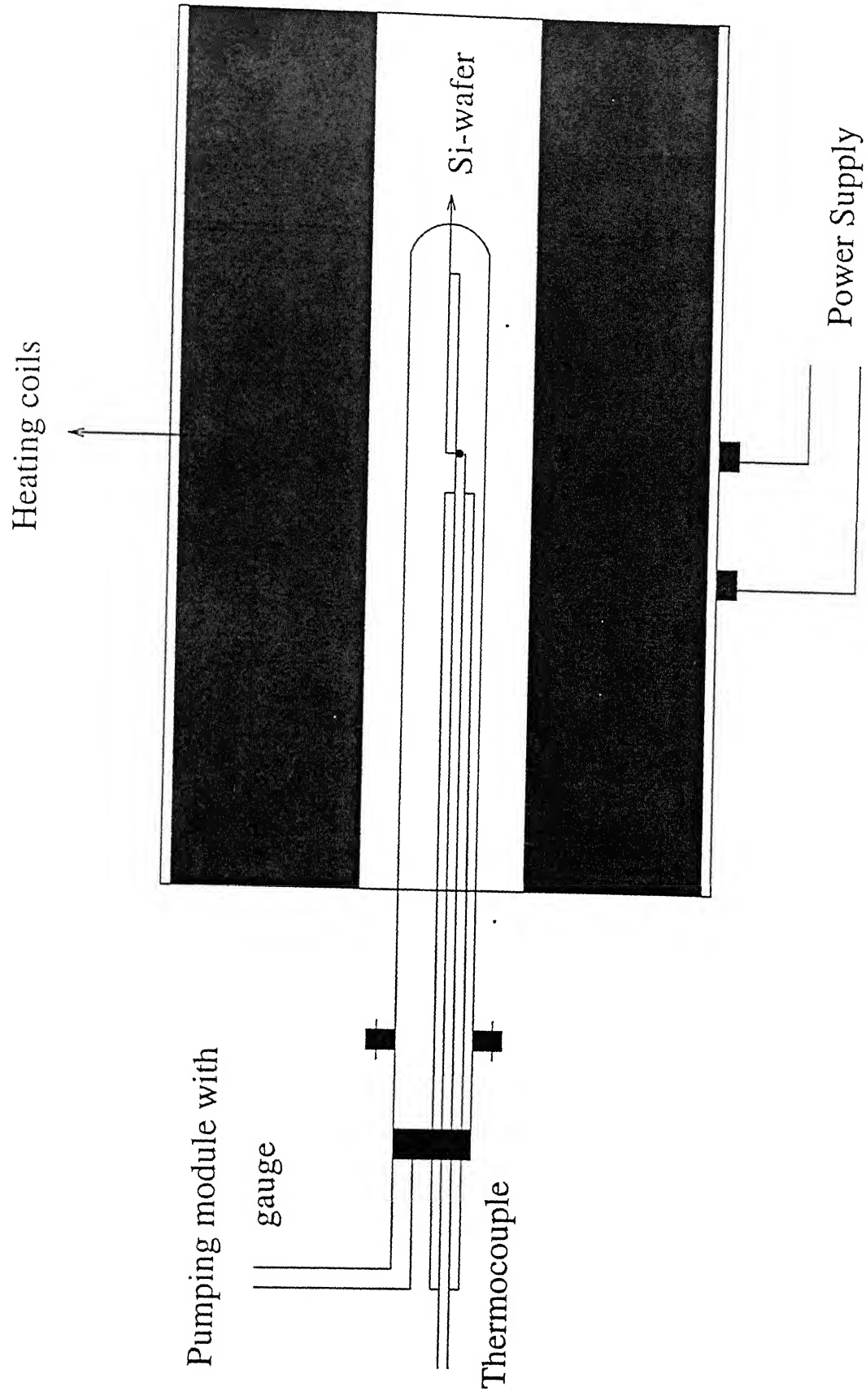


Fig.2.1.1 : Schematic diagram of annealing set-up

attained, the quartz tube was inserted into the furnace already maintained at the set temperature. After annealing for 0.5 h, the furnace was turned off and sample was left to cool down as such to room temperature. Finally, the pumping was shut down and the sample taken out for electrochemical etching. Fig 2.2 gives the flow diagram of substrate preparation steps.

### 2.1.2 Electrochemical etching

Fig 2.3 shows a schematic diagram of the electrochemical cell used for etching of c-Si. It consists of a teflon cylinder with a coaxial circular slot engraved for holding a mask to enable selective exposure of c-Si wafer. The mask is just a washer made of teflon. An O-ring is put inside the groove (around the central hole) to seal and prevent acid leakage. For etching, c-Si wafer is placed in the central slot on the mask with the face to be etched in contact. A brass disc fitted coaxially with a rod is polished well using a fine grade emery paper and is placed touching the aluminium coated c-Si for making electrical connection. Threads are made on the walls of teflon cylinder to fit a nylon nut having a through hole to accommodate the brass electrode. By tightening the nut, optimum pressure can be applied on the brass electrode to obtain a good electrical contact with the c-Si wafer. The entire assembly is placed into a nylon seat with the polished c-Si surface facing upwards. The nylon seat is also a hollow cylinder with a slot of diameter matching with the outer diameter of the teflon cell. The lower end of the nylon cylinder is provided with a notch for leads to complete the electrical circuit.

Table 2.1. Preparation conditions of porous silicon (PS).

Sample code	Resistivity of Si-substrate $\rho(\Omega\text{-cm})$	Etching Current ( $\text{mA}/\text{cm}^2$ )	Etching time (minutes)
PSL1	0.5-1.0	10.5	120
PSL2	0.5-1.0	10.5	90
PSL6	0.5-1.0	5.0	120
PSL11	0.7-1.5	5.0	15
PSL13	0.3-0.6	10.0	30

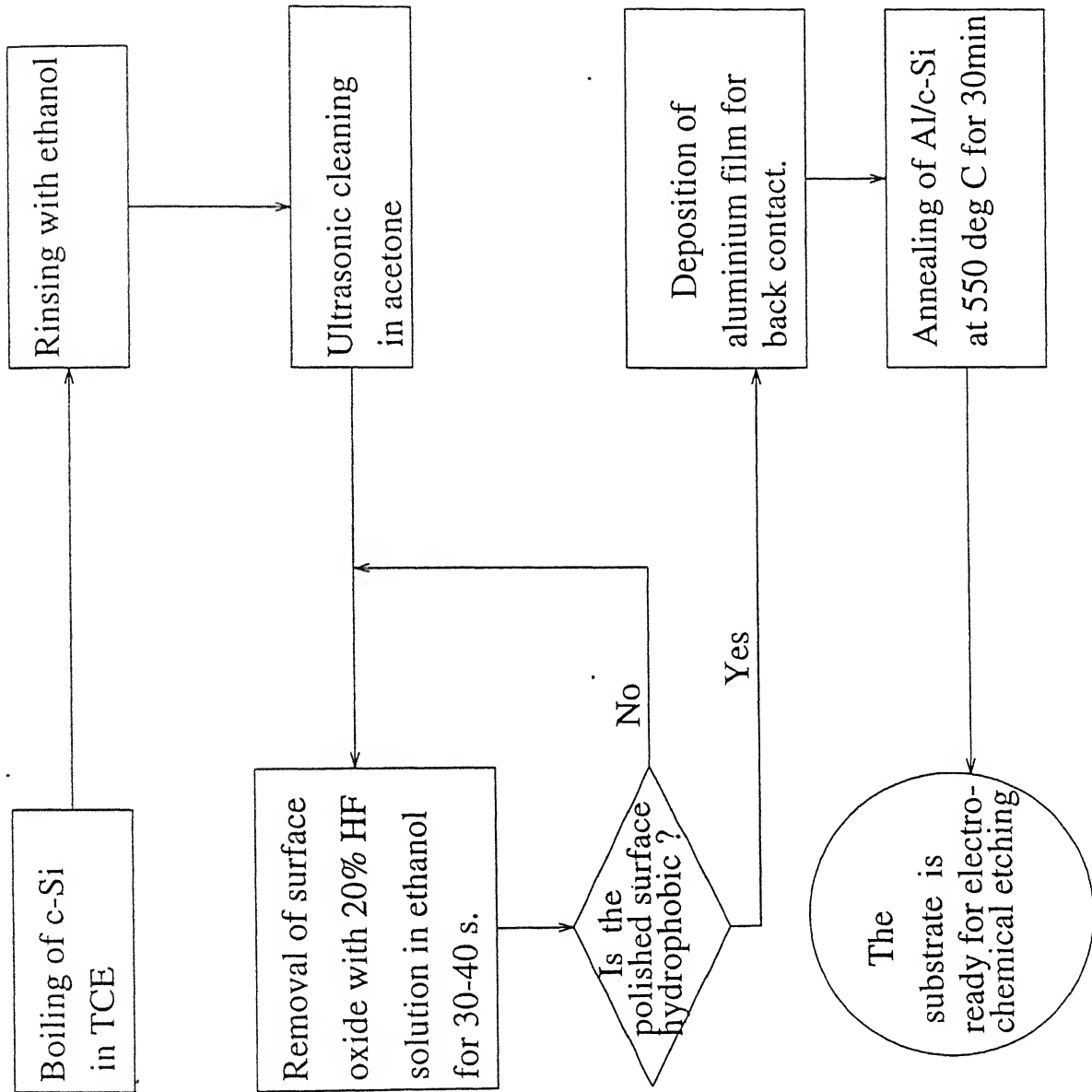


Fig.2.2 :Flow diagram of the substrate preparation steps.

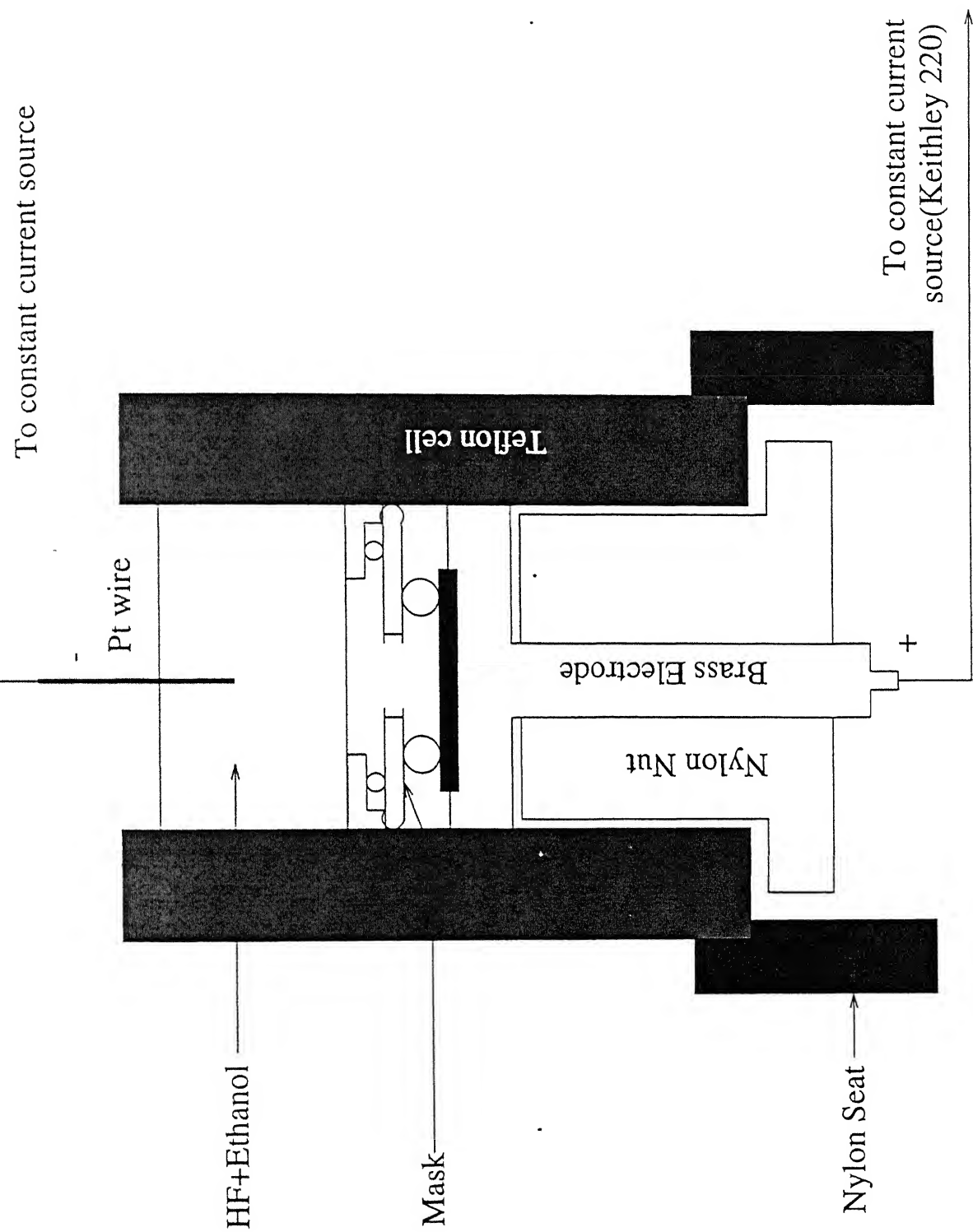


Fig2.3:A set-up for electrochemical etching of silicon.

The 1:1 mixture (by volume) of 48% HF and 99.9% C<sub>2</sub>H<sub>5</sub>OH is poured into the teflon cell. The whole set-up is mounted on a stand. A platinum wire immersed into the electrolyte serves as a cathode. A constant current is passed through the cell for anodization to occur at the exposed surface of the c-Si wafer. While Kiethley 220 programmable current source is used as the power supply, a Keithley 196 DMM monitored the voltage across the cell. The whole set-up is housed in a clean-bench to not only provide a dust free environment, but also, safeguard against the hazards of HF fumes. Initially, a high current (raising the density to 100 mA/cm<sup>2</sup>) is passed for about 10 s to electropolish and make the surface uniform. The current source is programmed before resuming etching. As the process begins, bubbles emerge at the substrate surface. According to Smith and Collins [37], SiH<sub>2</sub> gas evolves during bubbling and pore formation occurs in c-Si top layers. After etching, electrolyte is removed and both the c-Si wafer and the cell rinsed with de-ionized water for 10 minutes and dried. For a given concentration of HF, thickness of porous layer formed is determined by etching time itself. A beam of UV light (from 125 W mercury lamp) is then impinged onto the etched area to examine luminescence, if present. The resulting porous silicon samples indeed exhibited the typical red or yellowish red luminescence. The samples are stored in a desiccator in dark.

## **2.2 Characterization methods**

### **2.2.1 Raman scattering**

Raman effect basically refers to the emergence of radiation of wavelength/frequency other than the incident beam at some angles on interacting with certain molecules. The process involves inelastic scattering and is very sensitive to the vibrational modes of molecules/atoms. Also, the extent of change (or shift) in frequency depends upon the chemical structure of the molecules responsible for the scattering. Raman spectrum is commonly plotted in terms of wavenumber shifts with respect to the source (incident radiation) line. The shifts towards lower and higher energies are termed as stokes and antistokes; the intensity of antistokes line is appreciably smaller than the corresponding stokes lines. As discrete energy shifts are observed in the Raman spectra, they indicate the presence of quantized energy transitions. The shift is understood by assuming that the incident radiation on interaction with the sample causes polarization and energy retained momentarily (i.e., for 10<sup>-15</sup> - 10<sup>-14</sup> s) in the virtual state without involving transition to a higher electronic energy level. Fig 2.4 shows interaction of radiation with zero and first vibrational levels of ground electronic state. After retention, the species

return to their ground state with release of radiation in all direction with exactly the same energy as the source (shown by dashed arrows in Fig 2.4). However, the species may relax to the first vibrational level of the ground state (broad arrows in Fig 2.4). The frequency of light emitted in this transition will be less by a quantized amount ( $\Delta E$ ), i.e., difference in energies of ground and first vibrational levels. Thus,

$$\Delta E = h (\Delta \nu)$$

where  $\Delta \nu$  is the frequency shift observed in the Raman spectra and  $h$  is Planck's constant. On the other hand, when the molecule already in the first vibrational level goes to the virtual state by interacting with the incident radiation and return to the ground state will release energy more by an amount  $\Delta E$ . Since the probability of molecules being in first vibrational state is low than in ground state at room temperature, antistokes radiation is weaker than stokes.

It may be mentioned that both the Raman and the infrared spectra depend upon the same vibrational mode but arise from processes that are mechanistically different. While infrared absorption requires a change in dipole or charge distribution of the molecule and a direct transition, Raman scattering involves a momentary polarization of the molecule that ceases upon relaxation and emission. The effectiveness of Raman scattering thus depends upon the ease with which electrons of the bond can be distorted from the normal positions (i.e., polarizability of the bonds); polarizability decreases with increase in electron density and bond strength but decrease in bond length. The Raman shift, in fact, requires a change in polarizability rather than change in dipole moment - associated with the vibrational mode of the molecule. For example, the molecule such as nitrogen, chlorine or hydrogen has no dipole moment and so not active towards infrared absorption. But, the polarizability of the bond between the two atoms varies periodically in phase with the stretching vibrations reaching a maximum and minimum at the extreme and closest separations, respectively. A Raman shift corresponding in frequency to that of the vibrational mode thus results. Raman spectrum gives a spectroscopic signature of structure, symmetry and dynamical characteristics of molecules.

Porous silicon samples were examined in a SPEX-1877 Triplimate Raman spectrometer. For this, 20 mW light of 514 nm wavelength emanating from an  $\text{Ar}^+$  laser was focussed onto the sample with a spot size of 50  $\mu\text{m}$  and back scattered rays were collected by a lens, passed through a slit to a triple monochromator and finally to a

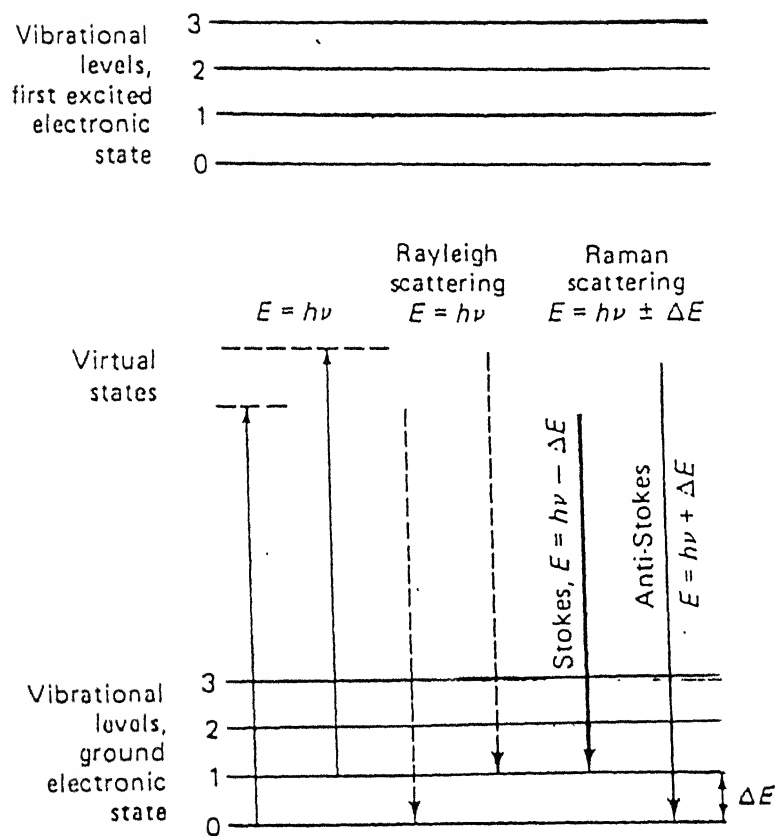


FIGURE 2.4 Origin of Raman spectra.

multichannel detecting system, consisting of charged coupled device (CCD) and photon counter. The CCD is cooled to liquid nitrogen temperature. The arrangement leads to a high sensitivity (quantum efficiency > 60%) with an extremely low background and noise level, thus enabling long accumulation time. The spectrum data is fed to a personal computer (PC) for storage, display and further analysis.

### 2.2.2 X-ray diffraction

Rich Siefert ISO - Debye flex 2002 X-ray diffractometer with  $\text{CuK}\alpha$  radiation  $\lambda = 1.5418 \text{ \AA}$  was employed to record the diffraction patterns and identify the phase (s) present in the porous silicon samples and changes occurring on annealing at  $250^\circ$ ,  $450^\circ$  and  $650^\circ\text{C}$ . The calibration of the system was carried out with a standard silicon sample. Further, the average size ( $t$ ) of crystallites present in the sample is evaluated from the X-ray line broadening [38]. Accordingly, the average crystallite size is given by the Scherrer relation

$$t = \frac{0.9\lambda}{B \cos \theta} \quad \text{with} \quad B = B_m - B_s$$

where  $\lambda$  is the wavelength of X-ray beam,  $B$  is the FWHM of diffraction peak (measured in radians) at a particular Bragg angle  $\theta$  (corresponding to  $2\theta$  in the diffractogram);  $B_m$  and  $B_s$  are FWHM of diffracted peaks obtained with the sample and the standard (c-Si, in the present case), respectively. The standard sample having a grain size  $> 0.2 \mu\text{m}$  is used to estimate the instrumental broadening and making correction in the experimental data.

### 2.2.3 EPR spectroscopy

Electron paramagnetic resonance (EPR) spectroscopy is based upon the absorption of microwave radiation by solids when placed in a strong magnetic field. Species that contain unpaired electrons are responsible for the absorption and therefore permit their detection. The electron has two energy levels, lower with spin quantum number  $m = -1/2$  and higher with  $m = +1/2$ . These energy levels split under influence of magnetic field ( $H_0$ ), such that their difference ( $\Delta E$ ) is given by

$$\Delta E = g \beta_N H_0$$



where 'g' is splitting factor and  $\beta_N$  is Bohr magneton ( $=9.27 \times 10^{-21}$  erg G<sup>-1</sup>). The value of 'g' for free electron is 2.0023 but varies with environment, e.g., is a few % of 2.0023 for unpaired electron in a molecule or ion. The value of  $\Delta E$  is  $6.3 \times 10^{-24}$  J or 0.03 meV in a magnetic field of 3400 gauss. This energy difference corresponds to frequency (e.g., 9500 MHz) that lies in the microwave region. The microwave radiation of frequency (say 9.5 GHz) emanating from source falls onto the sample held in a small quartz tube positioned between the pole of the permanent magnet. Helmholtz coils provide a means for varying the magnetic field over the small range ( $\sim 4$  Gauss, 100 KHz) in which the resonance occurs. The absorption of radiation can then be measured as a function of magnetic field. Generally, EPR spectra are recorded in derivative form of the Intensity vs. magnetic field data to enhance sensitivity and resolution. A Varian model E-109 spectrometer has been used in X-band to record the derivative microwave absorption spectra of virgin porous silicon samples (PSL 2 and PSL 6) and after annealing them upto 250<sup>o</sup>, 450<sup>o</sup> and 650<sup>o</sup>C. A standard sample of  $\alpha\alpha'$ -di phenyl- $\beta$ -picryl hydrazyl (DPPH) is employed to determine the 'g' factor of porous silicon using

$$g_{PS} = g_{DPPH} \times \frac{H_{o(DPPH)}}{H_{o(PS)}}$$

where  $g_{DPPH} = 2.0036$  at room temperature, and  $H_{o(DPPH)}$  and  $H_{o(PS)}$  are resonance magnetic field found in the EPR spectra of DPPH and PS, respectively. The signal parameters (viz., peak to peak width and height) are measured from the EPR spectra for the estimation of spin density as described later in chapter 3.

#### 2.2.4 Thermal gas effusion

Thermal gas effusion is employed to identify chemical species released on heating of porous silicon (PS) in vacuum. The set-up used for this purpose is shown schematically in Fig. 2.5. The porous silicon (PS) sample is placed in a quartz tube (inner diameter 1.44 cm and length  $\sim 18$  cm), connected to a quadrupole gas analyzer (QGA) and a turbo molecular pump (TMP). For temperature measurement, a chromel-alumel thermocouple is inserted into another quartz tube of inner diameter of 3 mm and placed by the side of the porous silicon (Fig. 2.5). Vacuum  $\sim 10^{-6}$  torr is created inside the quartz tube. The temperature is then raised to a particular level by switching on the furnace. The

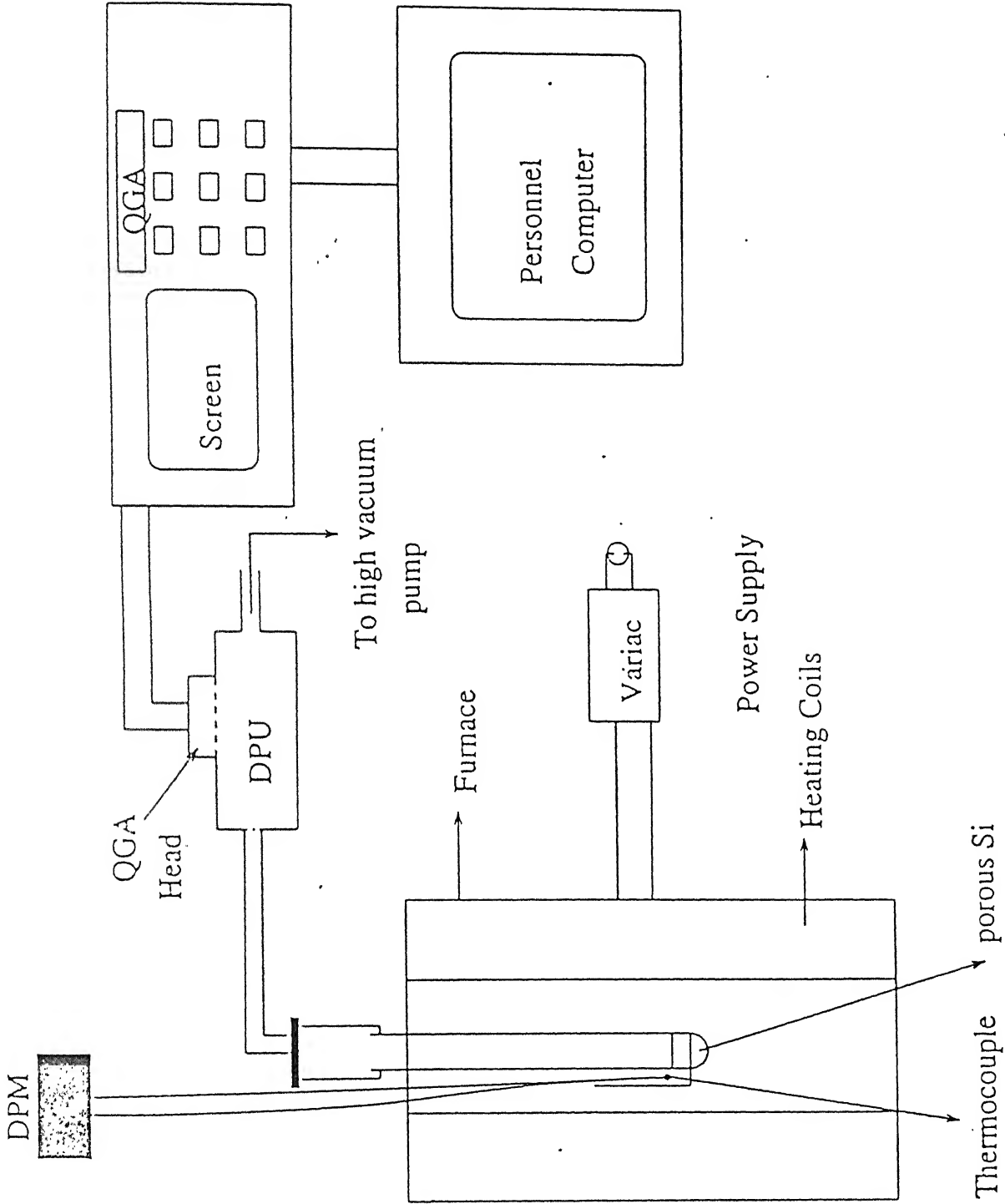


Fig. 2.5: Schematic diagram of Thermal Effusion Set-up  
DPM: Digital Panel meter DPH: Differential

gas evolved are analysed with a QGA by converting them into respective ions and measuring their  $m/e$  ratios.

A quadrupole gas analyzer (QGA) contains four short parallel metal rods arranged symmetrically around the ion beam (Fig. 2.6). The opposite rods are connected together, one pair is attached to the positive while the other to the negative of a d.c. power source. In addition, a radio frequency a.c. potential is applied to both the pairs. Neither field acts to accelerate the positive ions. The combined field, however, causes species to oscillate about their central axis of travel; only those with a certain mass-to-charge ratio can pass through the array without being removed by collision with one of the rods. Mass scanning is achieved by varying the frequency of the a.c. supply or changing the potential of the two sources while keeping their (frequency/potential) ratio constant. The ions which pass through are collected by an electrode, well shielded from stray ions, and current thus produced is amplified electronically and recorded. Ion current usually vary over a range of  $10^{-17}$  to  $10^{-9}$  A. QGA works in two modes : (i) the partial pressure of gases versus  $m/e$  ratio and (ii) partial pressure of gases (12 in number) as a function of time. In the present work, QGA is used in the first mode for various ions listed in Table 2.2. A personal computer (PC) was interfaced with QGA for monitoring the partial pressures as a function of temperature and storing the data.

Table 2.2 The ions traced in thermal effusion of porous silicon.

Serial no.	( $m/e$ ) of ions	Ions
1.	1	$H^+$
2.	2	$H_2^+$
3.	16	$O^+$
4.	29	$SiH^+$
5.	30	$SiH_2^+$
6.	31	$SiH_3^+$
7.	32	$O_2^+$
8.	47	$SiF^+$
9.	48	$SiFH^+$
10.	49	$SiFH_2^+$
11.	68	$SiF_2^+$
12.	87	$SiF_3^+$

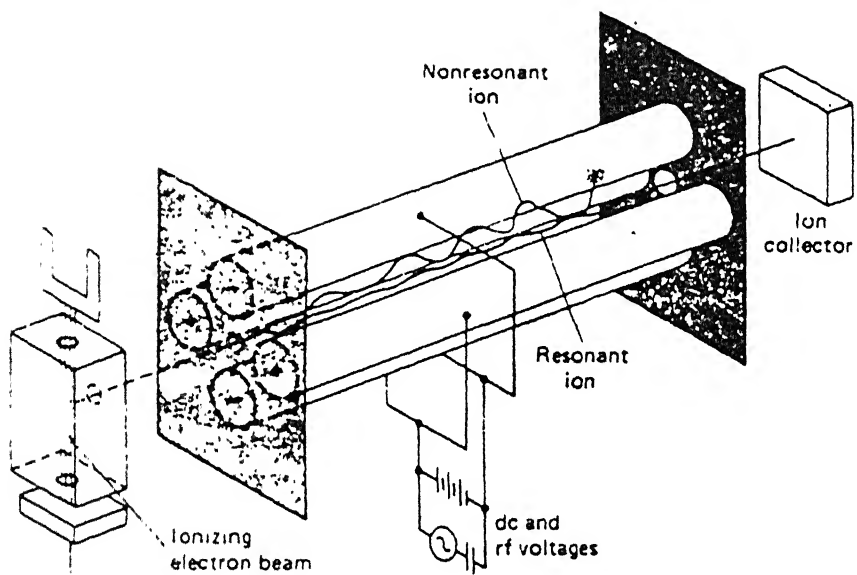


FIGURE 2-6 A quadrupole mass spectrometer

### 2.2.5 FTIR spectroscopy

The fourier transform infrared (FTIR) spectrometer is shown schematically in Fig. 2.7. The radiation from a broad-band light source is divided into two parts by a beam splitter. After reflection from a fixed and a movable mirror, respectively, the two partial waves are combined by the same beam splitter and focussed on a detector. They interfere there and yield the total intensity. For different positions of the movable mirror the two partial waves get different phase shifts with respect to each other. Therefore, on the detector the radiation field is superimposed with a time-delayed copy of itself. Hence, the detector signal resulting while the mirror moves is basically is the autocorrelation function of the radiation field (or interferogram). The fourier transform of this function gives the FTIR spectrum in the frequency domain. The spectral resolution in FTIR is determined by the inverse of the total path of the movable mirror. The light from all spectral intervals contributes to the detector signal and no mechanical slits are required here. These features reduce the time needed to record a spectrum considerably. FTIR spectra were recorded in the laboratory atmosphere using a 1760 - X Perkin - Elmer spectrophotometer in the wavenumber range of  $500 - 3600 \text{ cm}^{-1}$  with a resolution of  $0.1 \text{ cm}^{-1}$ . As aluminium itself absorbs infrared radiation, measurements were carried out after removing that from the back of the porous silicon. FTIR spectra were recorded for virgin samples (PSL2, PSL6 and PSL13) and again after annealing them upto  $250^{\circ}$  and  $450^{\circ}\text{C}$ .

### 2.3 Peakfit Analysis

For analysing the Raman spectra and thermal gas effusion data, a software package called “peakfit analysis” was employed. It is a menu driven package and therefore easy to use. In this, the data is first plotted, and then subjected to base-line correction and curve fitting with distributions such as Gaussian, Lorentzian, Voit, etc. Subsequently, by adjusting the width and the height of peaks, iterations performed until convergence is attained. The fitted curve then provides information about peak position, full width at half maxima (FWHM), percentage area under various peaks, etc. as discussed in chapter 3.

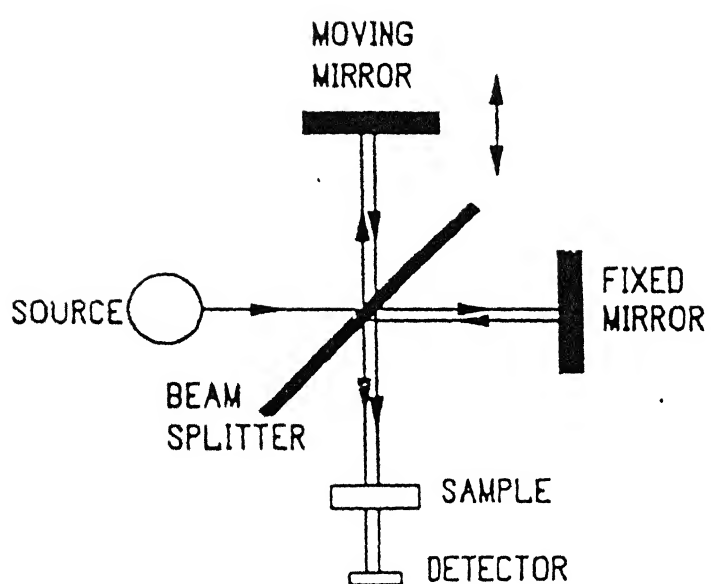


Fig. 2.7 Scheme of a Fourier transform spectrometer

### 3. Results and Discussion

In this chapter, we present the characterization results of porous silicon involving Raman, X-ray diffraction, electron paramagnetic resonance (EPR), thermal gas effusion and fourier transform infrared (FTIR) spectroscopic techniques. Also, the effect of annealing on the nature of PS sample is described using X-ray, EPR and FTIR data.

#### 3.1 Raman Spectroscopy

Fig. 3.1 shows a typical Raman spectrum of p-type c-Si together with the curve joining experimental data points. Its analysis carried out using a peakfit software package, as mentioned in chapter 3, gives deconvoluted plot depicted by dashed curve (not visible since superimposed on the experimental data curve of Fig 3.1). The central maxima occurs at Raman shift of  $520.1\text{ cm}^{-1}$  with a FWHM of  $7.0\text{ cm}^{-1}$ . It can be noticed that the peak is symmetric in nature. Also, the values obtained match well with the reported Raman data of c-Si wafers, i.e., the peak maxima and FWHM lying in the wavenumber ranges  $520\text{--}522\text{ cm}^{-1}$  and  $3\text{--}8\text{ cm}^{-1}$ , respectively [31,39-41]. According to Iqbal and Vepek [30], silicon films exhibit Raman spectra with peak maxima at progressively lower frequencies and larger FWHM besides increase in asymmetry (i.e., tail towards low frequency side) with decrease in grain size below  $200\text{ nm}$ . Raman spectrum of an a-Si contains usually a very broad and weak peak near  $480\text{ cm}^{-1}$  and is attributed to the vibrational density of states [30].

Raman spectra of virgin porous silicon samples PSL2, PSL6 and PSL13 recorded from two surface regions (say 'a' and 'b') of diameter  $50\text{ }\mu\text{m}$  each are depicted in Fig 3.2-3.4. While the experimental profiles are drawn by continuous curves, deconvoluted plots obtained for each are shown by three dashed Gaussian distribution functions. Table 3.1 gives summary of three peak maximas and their FWHM ranges for various Raman spectra (Fig 3.1-3.4). As can be noticed, the first peak (No.1) maxima lie within the wavenumber range  $519\text{--}521\text{ cm}^{-1}$  and therefore correspond to c-Si. However, widths of signal peaks emerging from region 'a' are relatively larger than from region 'b', which actually corresponds to more of crack portion and hence give contribution of the substrate itself. The larger FWHM of Raman peaks resulting from region 'a' can be attributed to both the microcrystallites present in PS and c-Si substrate. Red shifted peak (No. 2) within

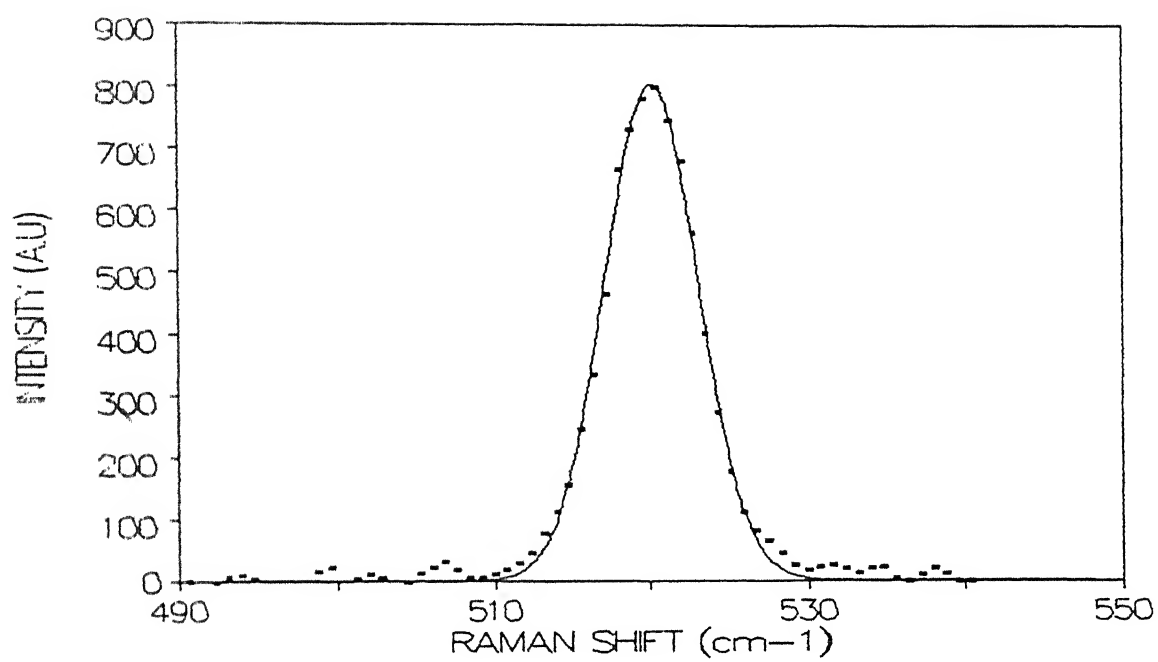


Fig. 3.1 Raman spectra of a standard c-Si.



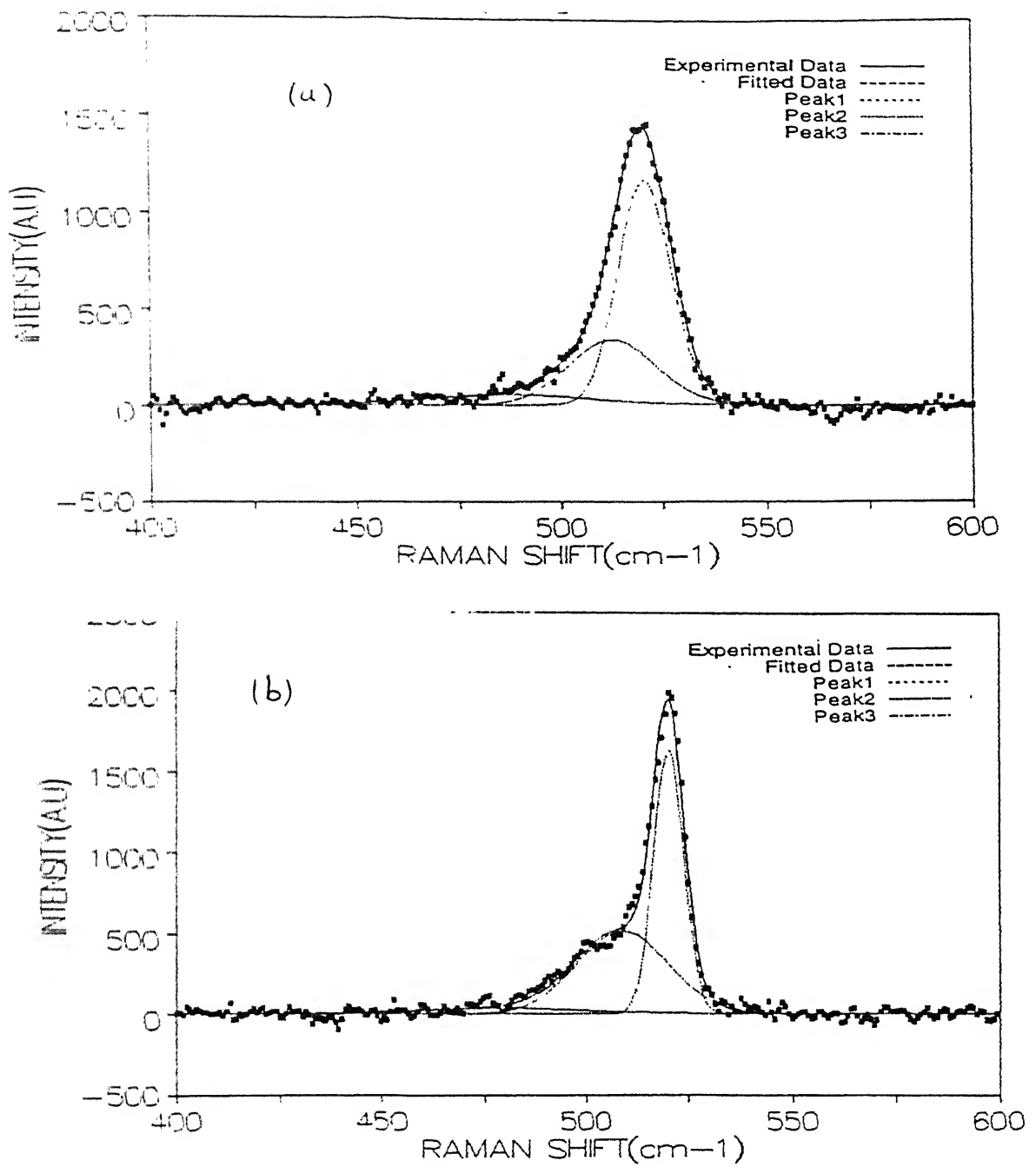


Fig. 3.2 Raman spectra of porous silicon PSL2 from two regions dominating : (a) solid structure and (b) crack.(or pores).

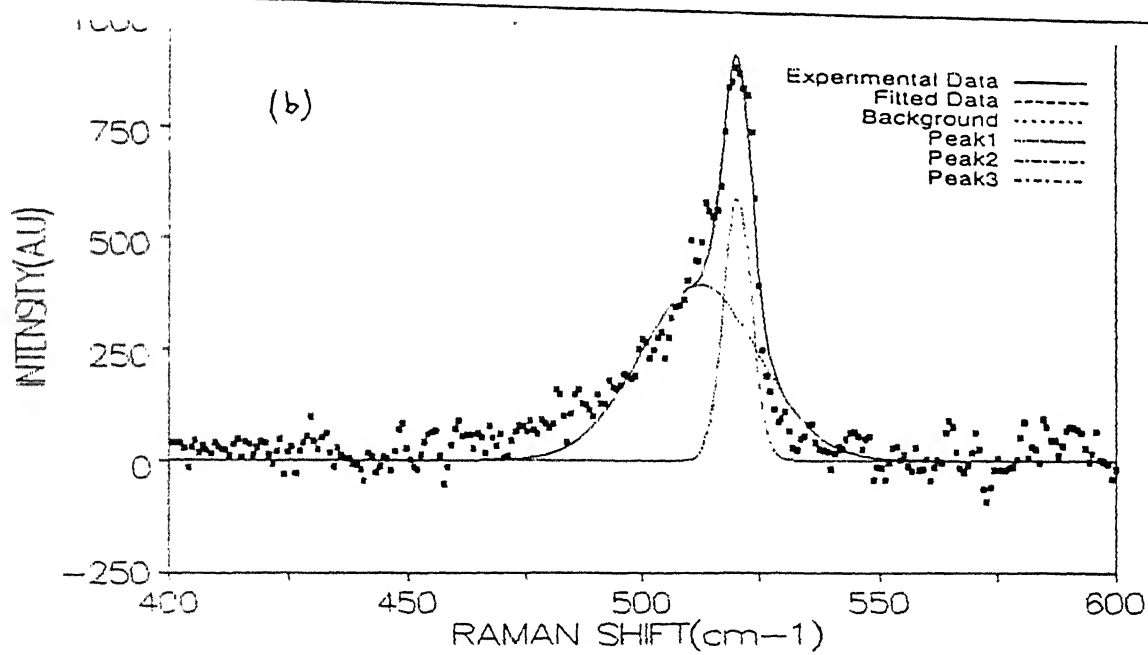
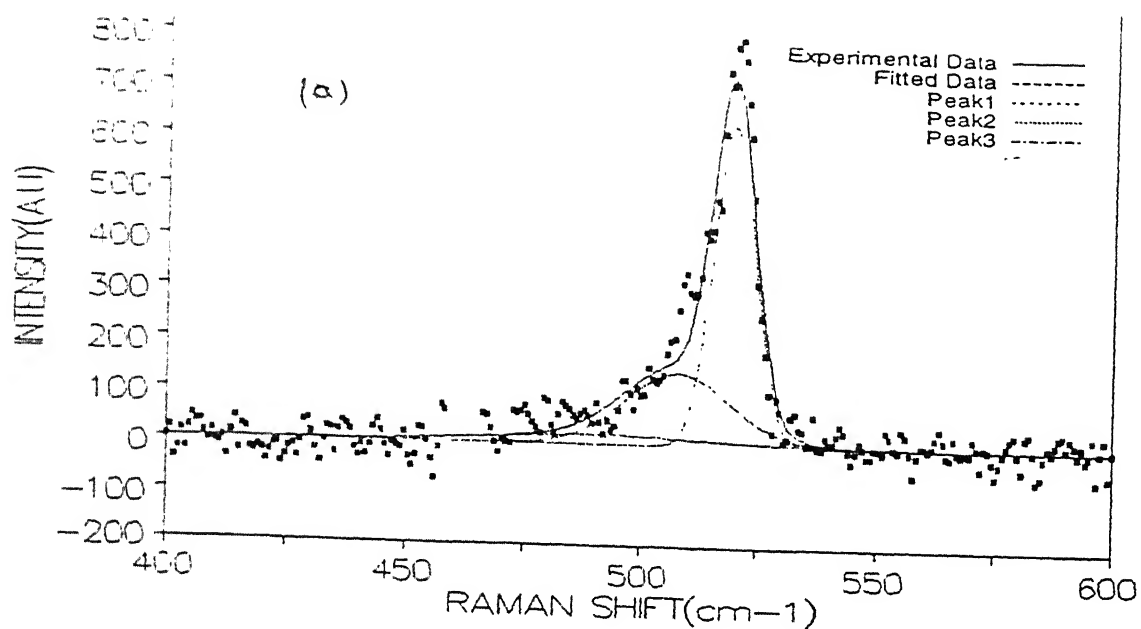


Fig. 3.3 Raman spectra of porous silicon PSL6 from two regions dominating : (a) solid structure and (b) crack.(or pores).

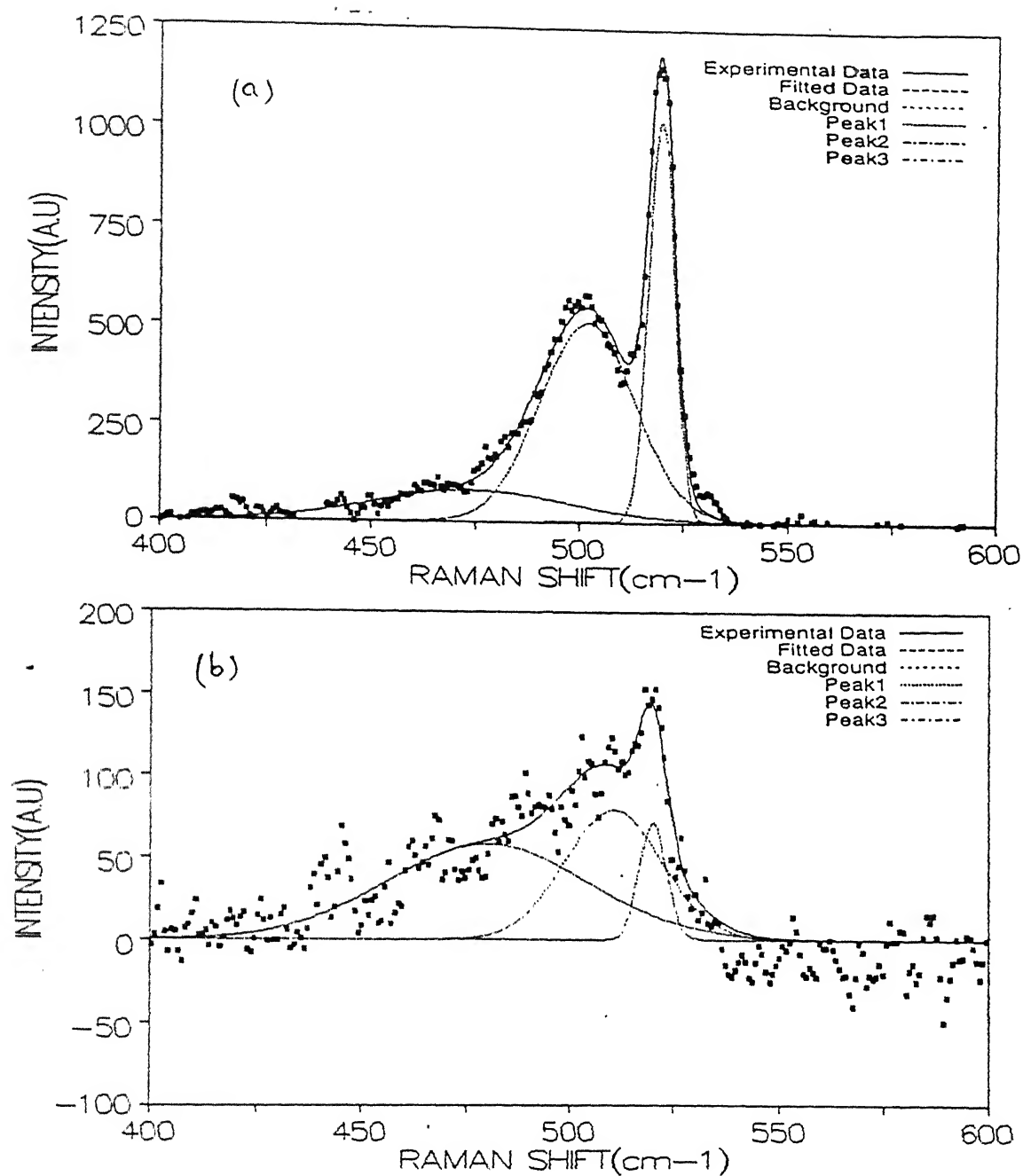


Fig. 3.4 Raman spectra of porous silicon PSL13 from two regions dominating : (a) solid structure and (b) crack.(or pores).

wavenumber range 502-513  $\text{cm}^{-1}$  having a larger FWHM of 23-28  $\text{cm}^{-1}$  is due to the nanocrystallites ( $< 5\text{nm}$ ) and therefore considered as characteristic of porous silicon [41]. These results indicate that porous silicon region is not homogeneous with regard to distribution of crystallites and pores. A very broad peak (No. 3) having FWHM in the range 48-61  $\text{cm}^{-1}$  and centred around wavenumber 473-490  $\text{cm}^{-1}$  appears because of the presence of disordered a-Si phase in porous silicon [39-41]. Asymmetry found in the Raman spectra towards lower wavenumbers itself suggest the existence of nanosized - Si crystallites in PS. It needs to be mentioned that annealing of PS makes the Raman spectra progressively symmetrical in nature as the crystallites grow in size in the process [42].

Table 3.1: Peak positions and their FWHM ranges for various Raman spectra shown in Figs. 3.1-3.4 of porous silicon.

Sample (location)		Peak 1		Peak 2		Peak 3	
		Position ( $\text{cm}^{-1}$ )	FWHM ( $\text{cm}^{-1}$ )	Position ( $\text{cm}^{-1}$ )	FWHM ( $\text{cm}^{-1}$ )	Position ( $\text{cm}^{-1}$ )	FWHM ( $\text{cm}^{-1}$ )
c-Si		520.1	7.0	-	-	-	-
PSL2	(a)	520.8	15.1	512.6	25	486.9	47.7
PSL2	(b)	520.3	8.6	508.8	26.5	479.1	48.3
PSL6	(a)	519.7	10.4	507.6	26.5	490.4	60.5
PSL6	(b)	520.3	3.0	512.2	22.6	-	-
PSL13	(a)	519.8	7.1	502.1	27.1	473.0	55.3
PSL13	(b)	520.0	6.6	510.5	27.5	479.9	56.9

The redshift and peak broadening observed in Raman spectra are usually attributed to the spatial confinement of optical phonon with decrease in crystallite size [43,44]. The optical phonons at nanosized crystallites do not correspond to plane waves and their localization causes relaxation in the wave vector  $q \approx 0$  selection rule. As a consequence, phonons of not only  $q=0$  but also  $q>0$  take part in Raman scattering process, resulting in the redshift and broadening of Raman peak. Fig 3.5 gives the redshift of PS as a function of FWHM. Clearly, the presented data (as found by others as well [45]) do not reflect any trend. Actually, phonon confinement model predicts a parabolic nature of such a plot [45].

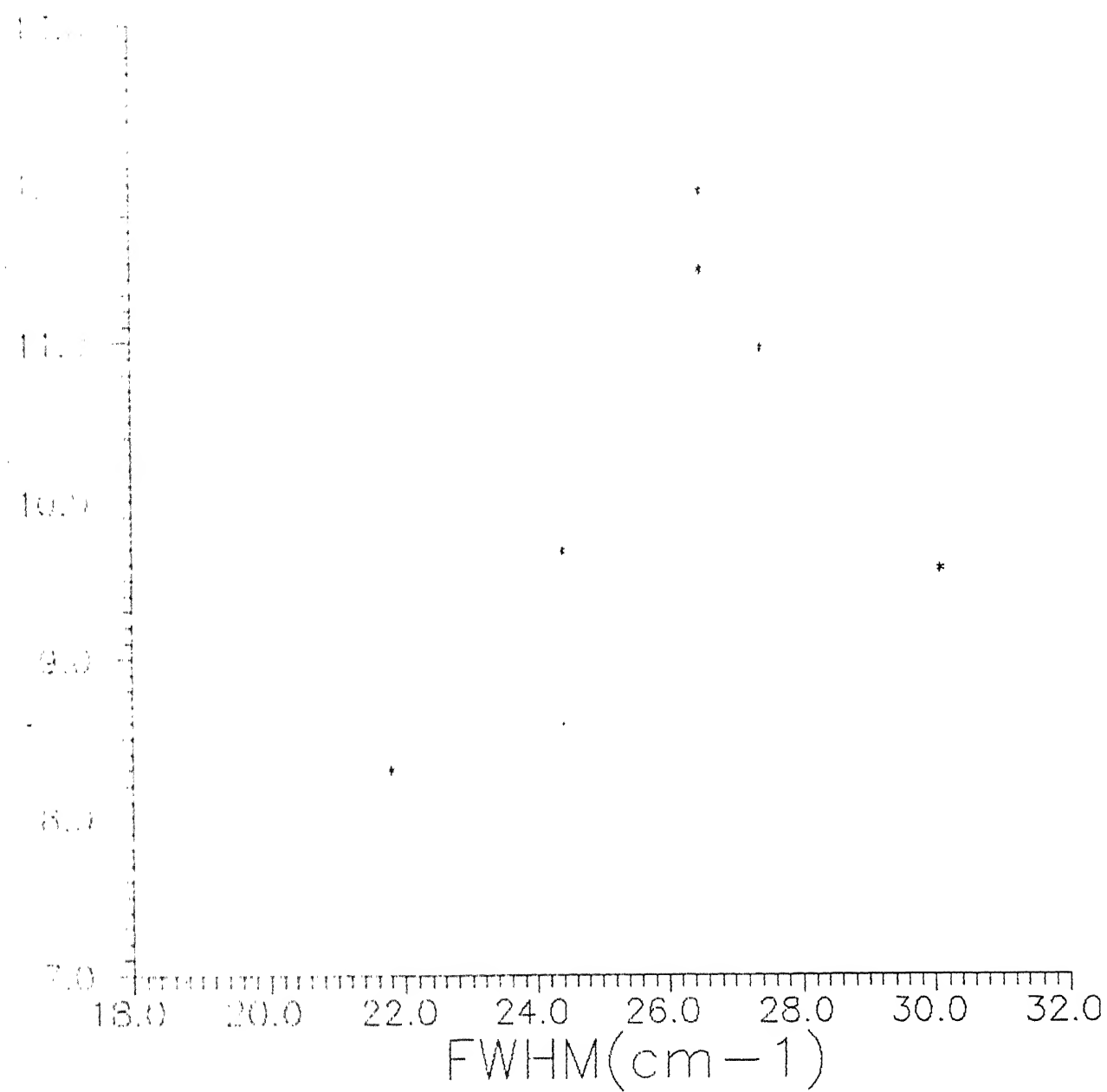


Fig. 3.5 The relationship between the redshift observed in PS with respect to that of c-Si and the FWHM of Raman resonance peak.

Yang et. al. [45] have, however, shown that phonon confinement description do not match with the experimental results. Instead, effect of strain (usually  $\sim 10^{-3}$ ) is also to be considered to account for the experimental data.

### 3.2 X-ray diffraction

Figs 3.6 and 3.7 show the X-ray diffractograms of porous silicon samples PSL2 and PSL6 in the  $2\theta$  range of  $58-78^\circ$  recorded with  $\text{CuK}\alpha$  radiation ( $\lambda = 1.5418 \text{ \AA}$ ). All virgin samples exhibit a broad peak around  $2\theta = 69.2^\circ$  which corresponds to 400 reflection of silicon. Needless to say, silicon wafers used for preparing PS had (100) orientation. Therefore, one expects reflections of h00 type only and the structure factor considerations limit those which satisfy  $h=4n$  ( $n$  being an integer). These observations (i.e., peak broadening and 400 reflection) indicate that crystallinities belong to diamond type silicon with lattice parameter  $a=5.4307 \text{ \AA}$ , are of nanometer size and maintain the orientation of the original silicon wafer. The line broadening data and corresponding average crystallite size determined (as described in section 2.2.2) are given in table 3.2.

After annealing at temperature at  $450^\circ$  and  $650^\circ\text{C}$  (see, e.g. Fig 3.6) of PSL2, 400 reflection peak becomes narrower with a sharp central maxima. It appears as if these are two peaks, originating from (i) c-Si substrate depicted by dashed curve and (ii) porous silicon shown by dotted curve, superimposed. Considering narrow peak for c-Si as standard and broad for PS, one can make corrections in the FWHM values and estimate changes in the crystallite size. The values thus obtained are also given in Table 3.2. These clearly show an increase in crystallite size by  $\sim 33$  and  $52\%$  at  $450^\circ$  and  $650^\circ\text{C}$ , respectively. The corresponding results with PSL6 samples reveal decrease in peak width without sharp central maxima found in PSL2 (Fig. 3.7). The crystallite size here increased by 25 and 50% at  $250^\circ$  and  $450^\circ\text{C}$ , respectively (Table 3.2). The difference in behaviour is caused as some portion of porous silicon region was lost in PSL2 during handling. This turned out to be advantageous as standard became available right on the sample itself and exactly at the diffraction angle  $2\theta = 69.2^\circ$ . The average crystallite size is invariably smaller in PSL6 mainly because of the longer etching time used [46]. As discussed later, effusion of hydrogen and other chemical species take place during annealing of PS. Consequently, average crystallite size should decrease. But, annealing also causes coarsening of particles. Since, an overall increase in crystallite size is observed, it can be inferred that process of coarsening predominates if effusion species rest on the surface only. Alternatively, the

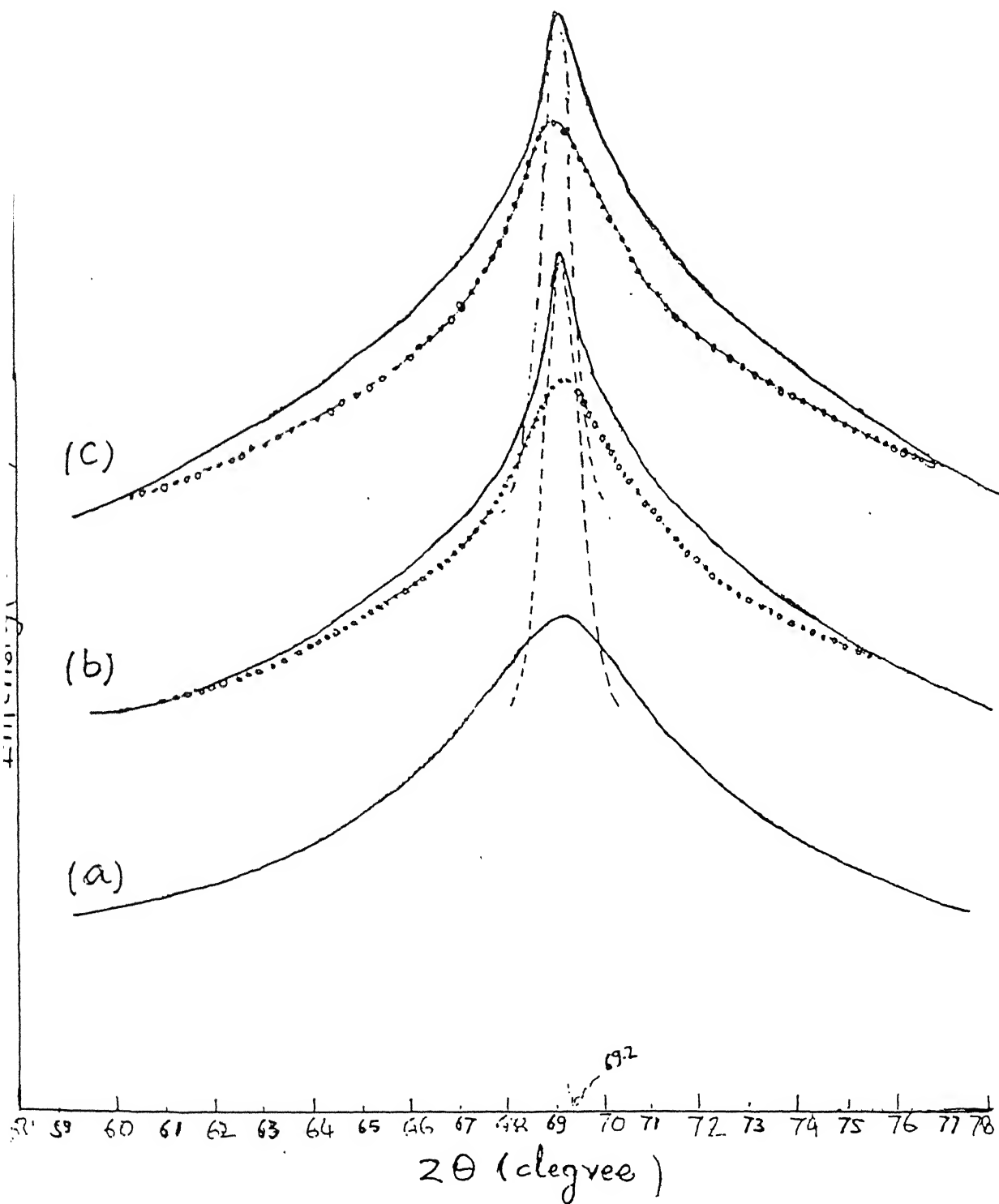


Fig. 3.6 X-ray diffractograms of PSL2 (a) in virgin state and after annealing upto (b) 450°C, and (c) upto 650°C.

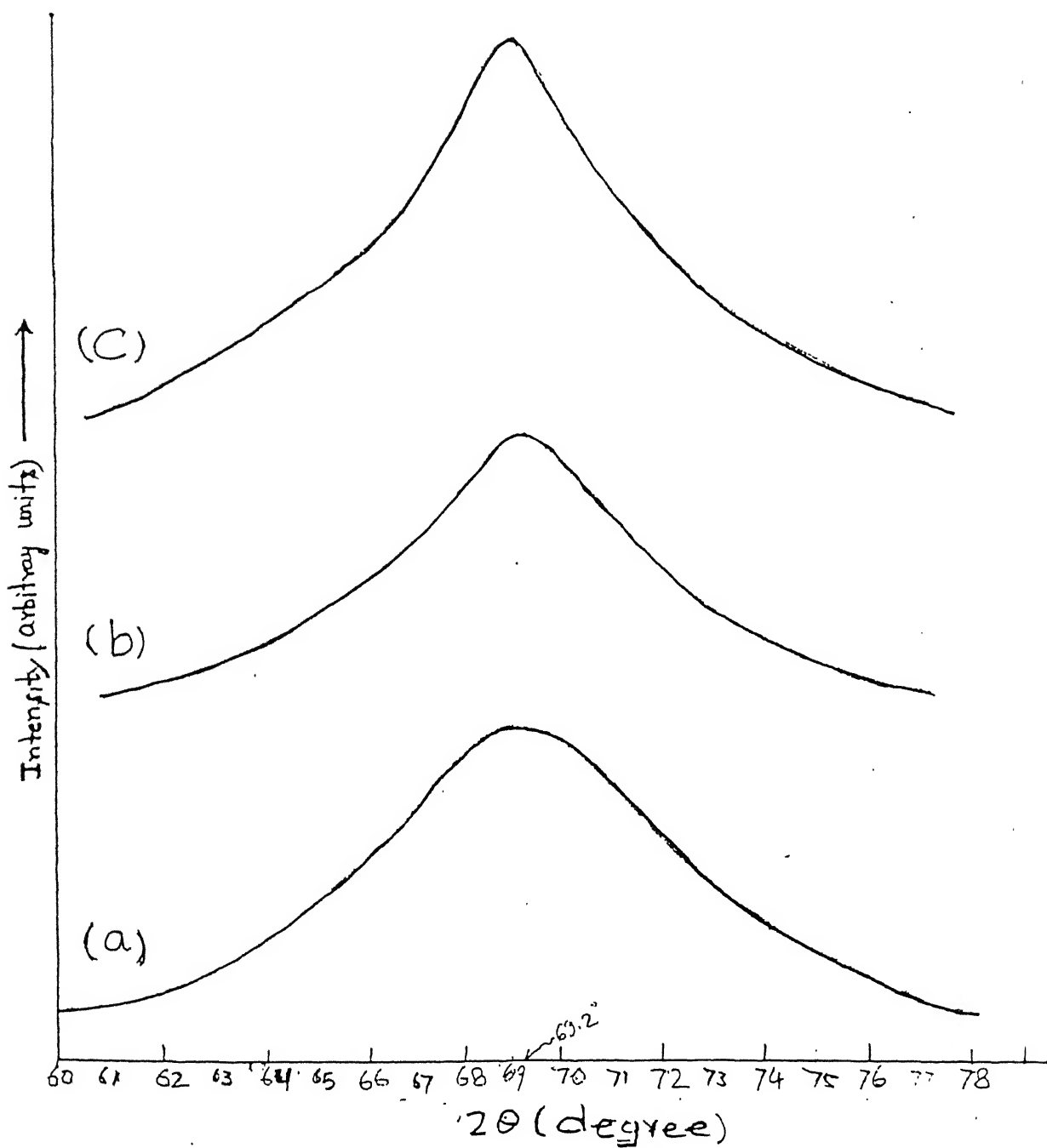


Fig. 3.7 X-ray diffractograms of PSL6 (a) in virgin state and after annealing upto (b) 250°C, and (c) upto 450°C.



crystallites must turn porous thereafter. Also, the crystallites continue to maintain preferred orientation (100) even after annealing atleast upto 650°C.

Table 3.2: X-ray line broadening data of porous silicon with average size of crystallites.

Sample	Virgin/ annealing temperature (°C)	2θ (degree)	B <sub>m</sub> (degree)	B <sub>s</sub> (degree)	B (degree)	Average crystallite size (t) (nm)
PSL2	Virgin	69.2	5.5	0.9	4.6	2.1
	450	69.2	4.4	0.9	3.5	2.8
	650	69.2	3.9	0.9	3.2	3.2
PSL6	Virgin	69.2	7.0	0.9	6.1	1.6
	250	69.2	5.8	0.9	4.9	2.0
	450	69.2	5.0	0.9	4.1	2.4
B <sub>m</sub> and B <sub>s</sub> are FWHM of diffraction peak of PS, and c-Si; respectively;						
$B = (B_m - B_s), \quad t = \frac{0.9\lambda}{B \cos \theta}; \quad \lambda = 1.5418 \text{ \AA}$						

### 3.3 Electron paramagnetic resonance (EPR) spectroscopy

The electron paramagnetic resonance technique is particularly suited for the studies of bulk, surface and interface defects in Si [47,48]. The EPR signal must come from the porous Si layer as it is observed in anodized samples and not in the original Si wafers. When the porous layer is thinned artificially by polishing, the intensity of the signal reduces progressively, which means that the spin centres are associated with the porous layer itself. Also, the detectable signal is found not only, to be, identical in the various porous layers, but also, independent of the substrate resistivity, substrate orientation and anodization conditions [49]. All these results confirm that the EPR signal is intrinsic to the porous Si. The following arguments are pertinent and useful for associating the EPR signal to Si dangling bonds.

- (a) From the previous EPR data of defects in c-Si, such as the phosphorus-vacancy pair [50], the five-vacancy cluster [51], the nitrogen-vacancy pair [52], and the  $P_b$  centre at the Si/SiO<sub>2</sub> interface [53], we find that the g-tensor is either exactly or approximately trigonally symmetric (axial direction  $\langle 111 \rangle$ ) (or deviating a little, usually by  $\sim 3^\circ$ ). Moreover, these defects have their spin electrons localized at Si dangling bonds which are oriented along  $\langle 111 \rangle$  directions. The slight deviation from  $\langle 111 \rangle$  may be caused by perturbation due to impurity or other lattice defects present near the dangling bond. Obviously, trigonal symmetric EPR signal can be identified with Si- dangling bonds in c-Si.
- (b) The principal g values obtained experimentally in respect of various defects whose spin electrons are localized at Si dangling bonds are listed in table 3.3. It is noticed that the value of  $g_{||}$  and  $g_{\perp}$  lie in ranges 2.0005-2.0026 and 2.0081-2.0110, respectively. Watkins and Corbett et al [50] have also found theoretically  $g_{||}=2.0023$  (which matches with free electron case) and  $g_{\perp} \simeq 2.010$  for unpaired electrons associates with Si-dangling bonds.

Table 3.3: Comparison of EPR g-values for spin centres consisting of an unpaired electron at a Si-dangling bond.

Identity		$g_{  }$	$g_{\perp}$	Refs.
c-Si	phosphous vacancy	2.0005	2.0104	[50]
	five vacancy	2.0020	2.0110	[51]
	Nitrogen-vacancy	2.0026	2.0089	[52]
Si/SiO <sub>2</sub>	$P_b$ center	2.0012	2.0081	[54]
Interface		2.0013	2.0090	[53]
Porous silicon	Dangling bonds	2.0023	2.0086	[55]

The effective g-values determined from EPR spectrum for the porous silicon PSL2 and PSL6 are found to between 2.0061 and 2.0067. In bulk c-Si, the dangling bonds may possess their axial directions along four equivalent  $\langle 111 \rangle$  axes [50-52], while at the (111) Si/SiO<sub>2</sub> interface, they are mostly aligned along direction perpendicular to interface [49,53,54]. However, for (100) Si/SiO<sub>2</sub> interface, dangling bond direction will be inclined to the interface normal [100]. So, their contribution to the EPR signal is expected to be anisotropic. That is perhaps the reason for our obtaining g-values in between the  $g_{||}$ ,  $g_{\perp}$  and  $g_{\text{eff}}$  as effective. On the other hand, the dangling bonds in an a-Si can not have

such an orientation disposition because of the absence of a regular or spatially coherent network. Previous and present results of Raman spectroscopy have revealed an amorphous region near the top layer of the porous silicon with characteristic peak at  $480\text{ cm}^{-1}$ . The contribution of the amorphous state to EPR, if exists, must be isotropic in nature.

Due to the low spin electron density in c-Si, their detection in bulk samples of a few  $\text{mm}^2$  size has not been possible. However, in the case of porous silicon, there is large internal surface area and so total spin number may become adequate to give a detectable EPR signal. Therefore, the properties of the  $\text{P}_b$  centre can possibly be used to characterize the internal surface of porous silicon. Finally, thermal annealing at  $250^\circ$ ,  $450^\circ$ , and  $650^\circ$  under ultrahigh vacuum may determine the importance of hydrogen passivation of  $\text{P}_b$  centres in the virgin samples. Both virgin samples PSL2 and PSL6 yield EPR signals. Figs 3.8 and 3.9 show room temperature EPR spectra of PSL2 in virgin state and after annealing upto  $450^\circ\text{C}$  at a rate of  $9.6^\circ\text{C}/\text{min}$  for 2 hours as a function of the magnetic field perpendicular to the sample surface (i.e., along [100], direction). It can be noticed that the line shapes are almost Lorentzian. Also, the line widths of the first derivative absorption spectra are 6.7G and 6.0G for PSL2 and PSL6, respectively. The principal value of g tensor in virgin state of samples were determined as  $g_{\text{PSL2}} = (2.0061 \pm 0.0002)$  and  $g_{\text{PSL6}} = (2.0067 \pm 0.0002)$ . In PSL2, two peaks were observed in the EPR spectra after annealing at  $650^\circ\text{C}$  and so the corresponding g-values determined are  $g_{\parallel} = 2.0073$  and  $g_{\perp} = 2.0035$ . The effective g-values was obtained from

$$g_{\text{eff}} = \sqrt{(g_{\parallel}^2 + 2g_{\perp}^2) / 3} \quad \text{as } 2.0045. \quad \text{The result of EPR studies are}$$

summarized in table 3.4. It is evident that the signal increases upon annealing in both PSL2 and PSL6, indicating the increase in the number of dangling bonds. The spin numbers (I) is calculated using the formula

$$I = KW^2H$$

where W is the peak width and H is peak height of signal in derivative mode and K is a constant. The values of K for line shapes in respect of Lorentzian and Gaussian distributions are 1.81 and 0.52, respectively. The standard DPPH sample is assigned a value of 1.1 for the constant K. Fig 3.10 shows the variation of 'g' values with the annealing temperature. It is clear that g-values change somewhat upon annealing but remain in between 2.0033 and 2.0067. Fig. 3.11 demonstrates that the peak width increases continuously from 6.7 to 7.5 G upon annealing of PSL2. However, the changes

Scan time : 30 min.  
 Time constant : 2 sec.  
 Modulation : 4 G for PS 2 1 G for DPPH.  
 Amplitude :  
 Receiver gain :  $10^5$   
 Microwave : 100 mW.  
 power

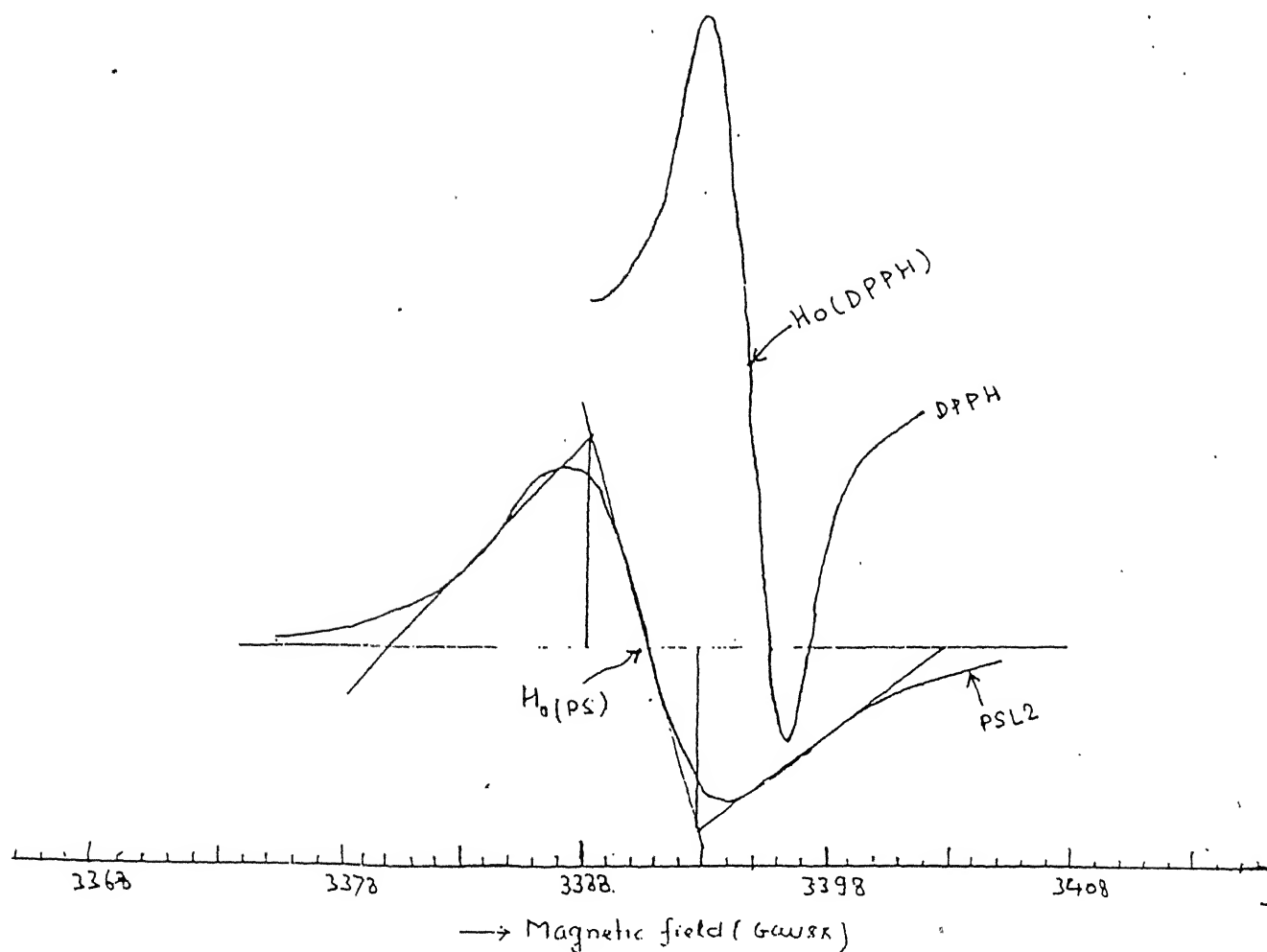


Fig. 3.8 EPR spectrum of PSL2 in virgin state and the standard DPPH sample.

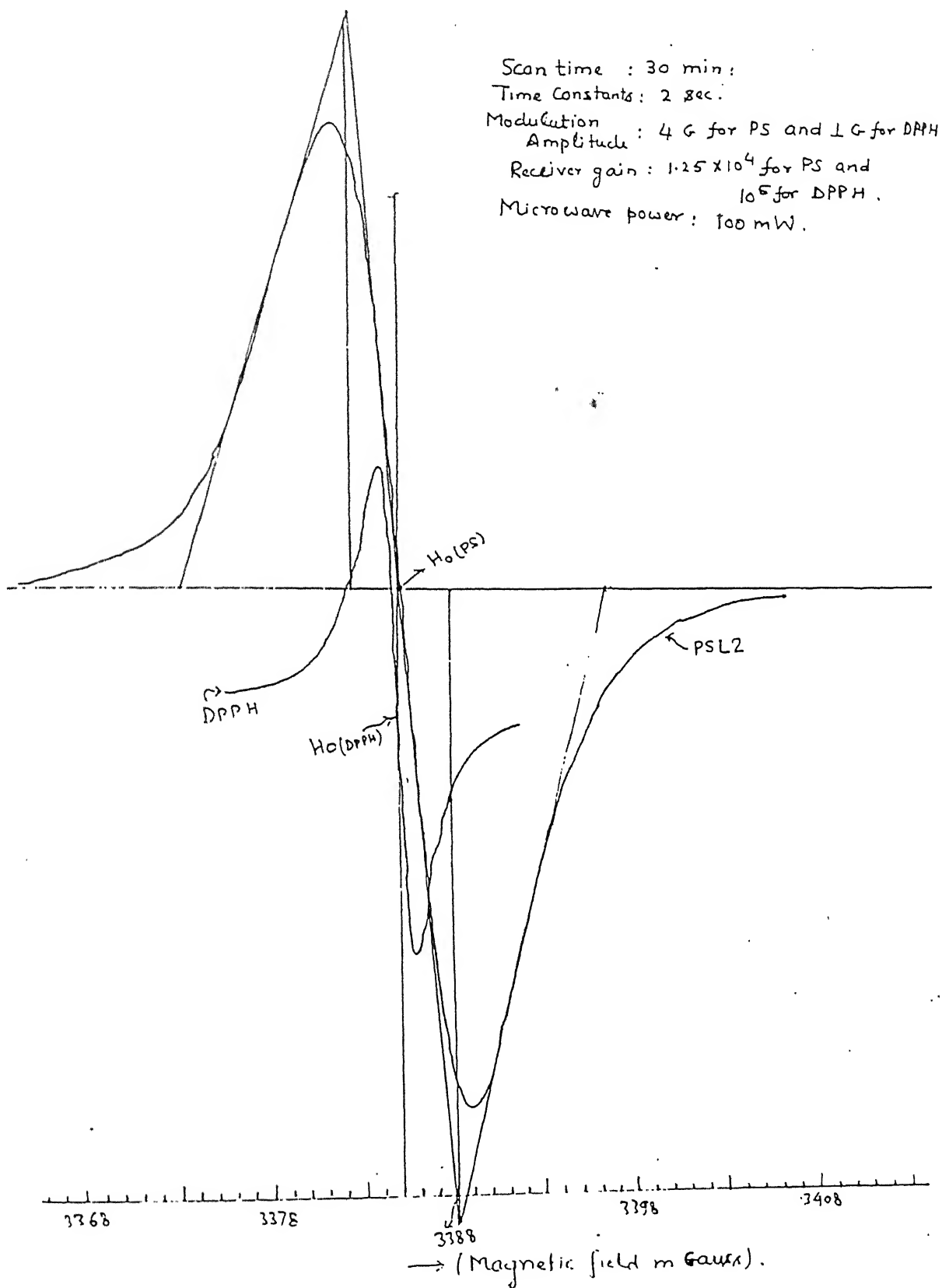


Fig. 3.9 EPR spectrum of PSL2 after annealing upto  $450^\circ\text{C}$  and the standard DPPH sample.

are erratic for PSL6. Fig. 3.12 depicts the relative spin numbers vs. annealing temperature plot. Obviously, the spin number increases to 45 times for PSL2 after annealing at 450°C and 10 times for PSL6 at 650°C. It means that the dangling bonds are indeed created upon annealing.

The thermal gas effusion data (discussed in section 3.4) indicate that the hydrogen and hydride species ( $\text{SiH}_x$ ) are evolved during annealing. This may produce dangling bonds, resulting in an increase in the EPR signal, as observed here. These results are in qualitative agreement with those reported earlier [50,53].

Table 3.4 Effect of annealing on EPR signal and related parameter in porous silicon.

Sample	Annealing temperature (°C)	g-values ( $\pm 0.0002$ )	peak width W (Gauss)	Height of signal (H) (arbitrary unit)	$W^2H$	Spin numbers (arbitrary unit)	Spin number relative to the virgin state
PSL2	Virgin	2.0061	6.7	26	1167	1167	1.0
	450	2.0033	7.5	954	5366	53662	46.0
	650	2.0045 effective	two peaks	-	-	-	-
PSL6	Virgin	2.0067	6.0	56	2016	2016	1.0
	250	2.0063	5.0	37	925	925	0.5
	450	2.0064	6.0	225	8100	8100	4.0
	650	2.0063	5.5	614	1858	18581	9.5

### 3.4 Thermal gas effusion

The gas effusion from porous silicon PSL1 and PSL11 samples annealed at the rate of 9.6°C per minute under clean vacuum  $\sim 10^{-6}$  torr was monitored by instant partial pressure at various temperatures and setting m/e numbers for  $\text{H}^+$ ,  $\text{H}_2^+$ ,  $\text{O}^+$ ,  $\text{SiH}^+$ ,  $\text{SiH}_2^+$ ,  $\text{SiH}_3^+$ ,  $\text{O}_2^+$ ,  $\text{SiF}^+$ ,  $\text{SiFH}^+$ ,  $\text{SiFH}_2^+$ ,  $\text{SiF}_2^+$  and  $\text{SiF}_3^+$  in a quadrupole gas analyzer (QGA). Figs. 3.13 and 3.14 show the gas effusion spectrum as a function of temperature for samples PSL1 and PSL11, respectively. The partial pressure of gas species is invariably larger in PSL1 presumably due to thicker layer of porous silicon as etching performed for longer time (120 m) against 15 m for PSL11. The assignments of various m/e numbers is based on the likely evolution of chemical species and their cracking patterns. For example,

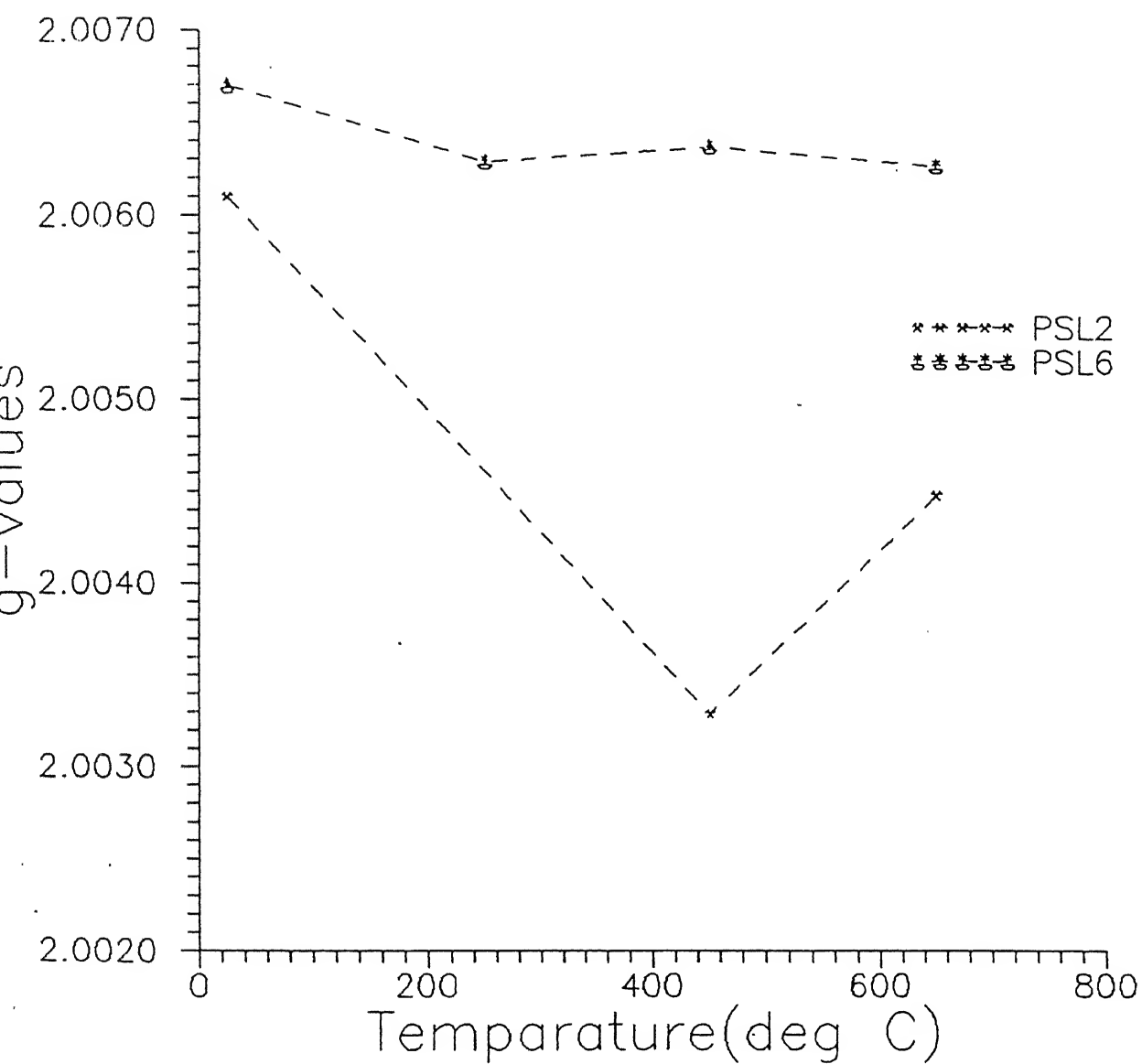


Fig 3.10 The variation of 'g'-values as a function of annealing temperature in porous silicon.

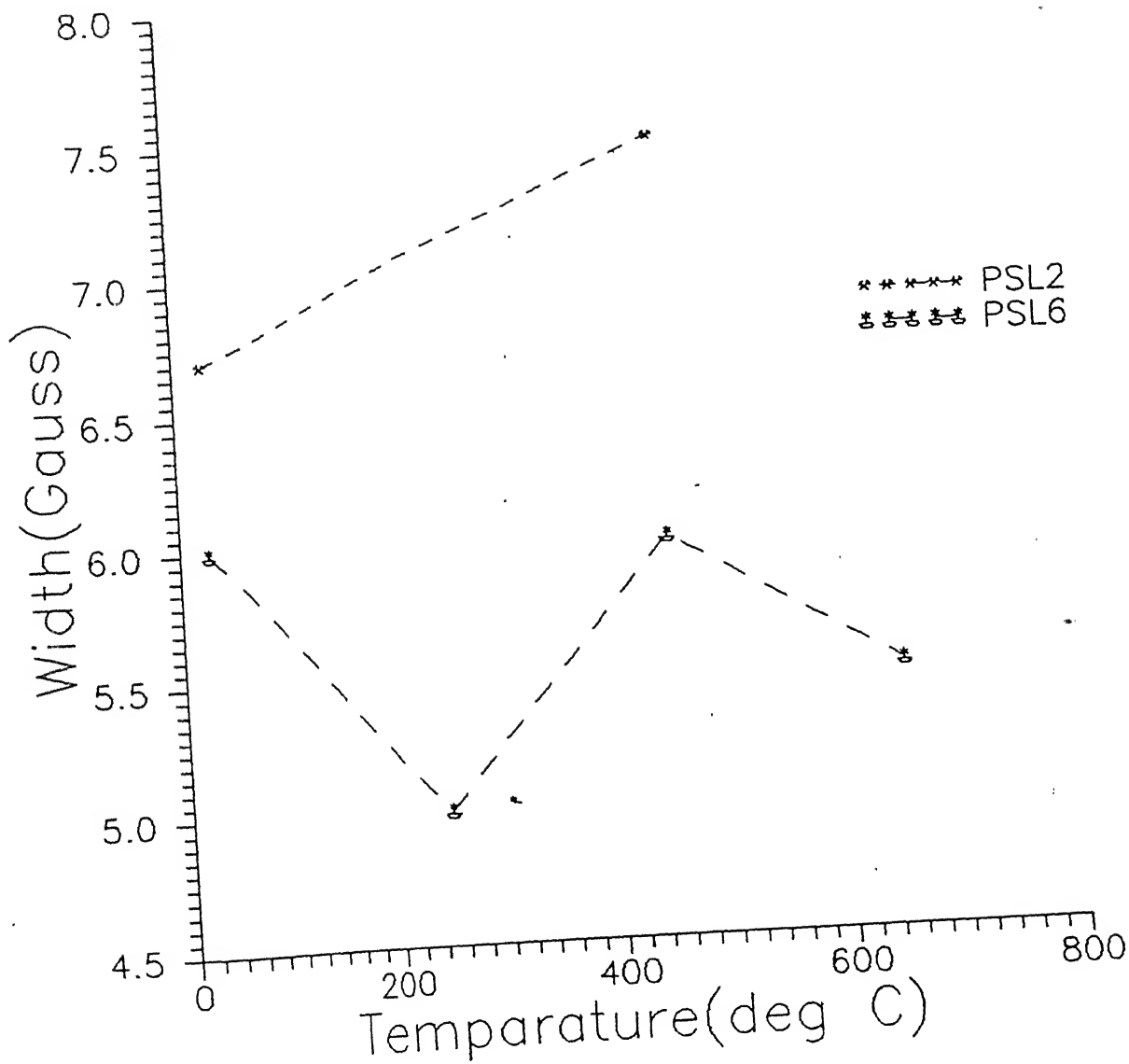


Fig. 3.11 A graph between EPR peak width and annealing temperature in porous silicon.



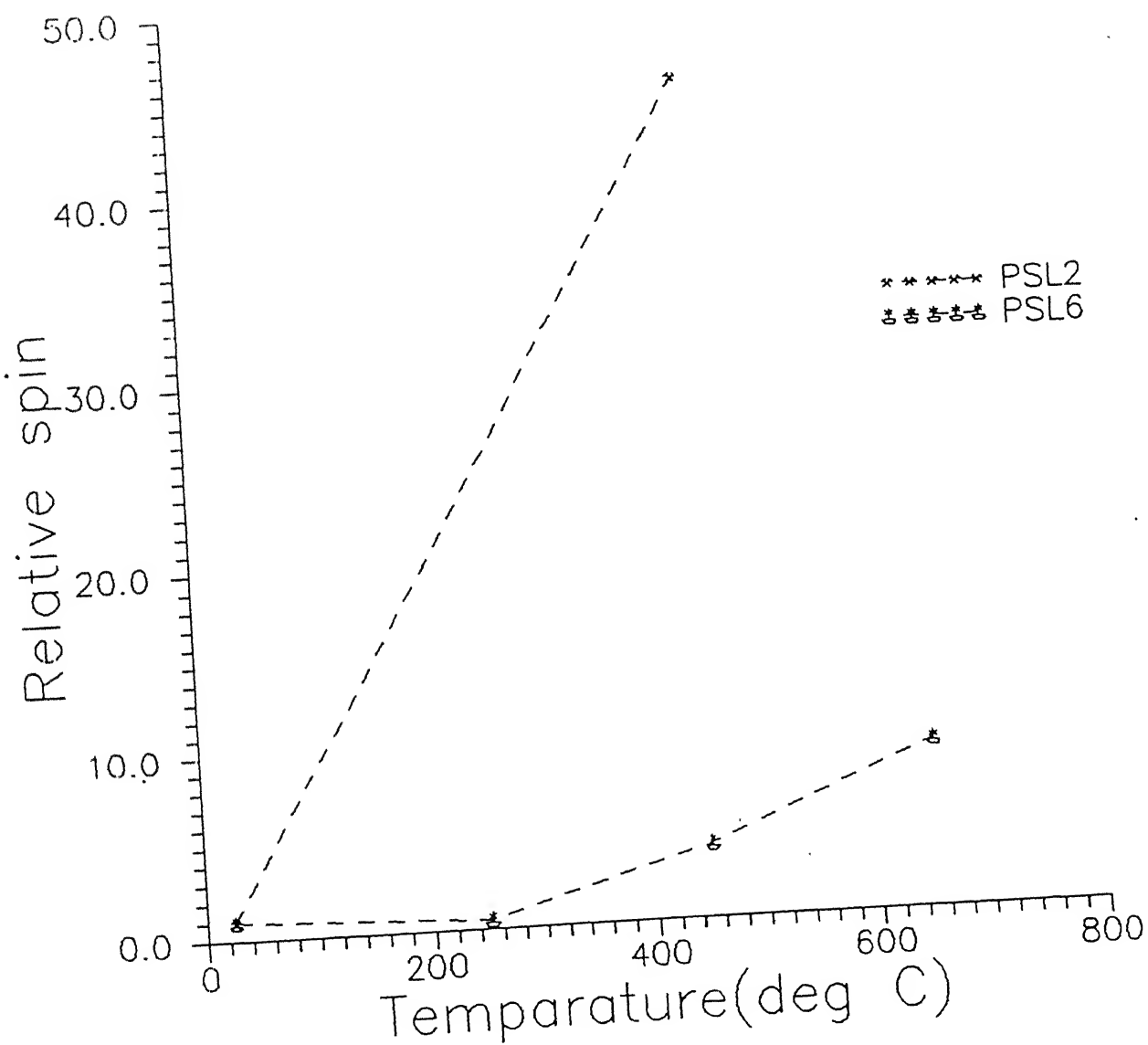


Fig. 3.12 A graph between spin numbers and annealing temperature in porous silicon.

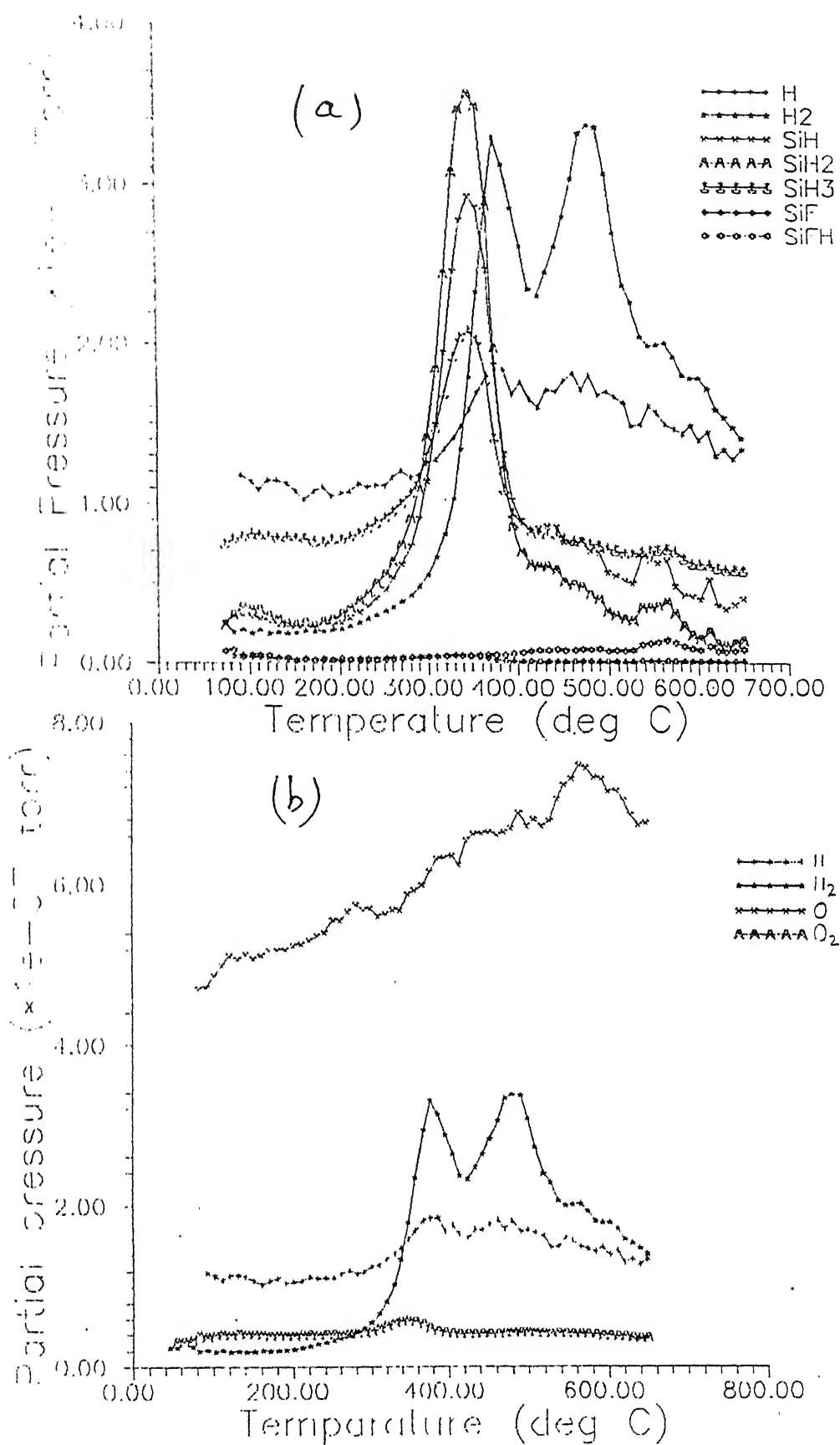


Fig. 3.13 Thermal gas effusion spectrum of PSLI as a function of temperature:  
For (a) H, H<sub>2</sub>, SiH, SiH<sub>2</sub>, SiH<sub>3</sub>, SiF and SiFH and (b) H, H<sub>2</sub>, O, O<sub>2</sub> species.

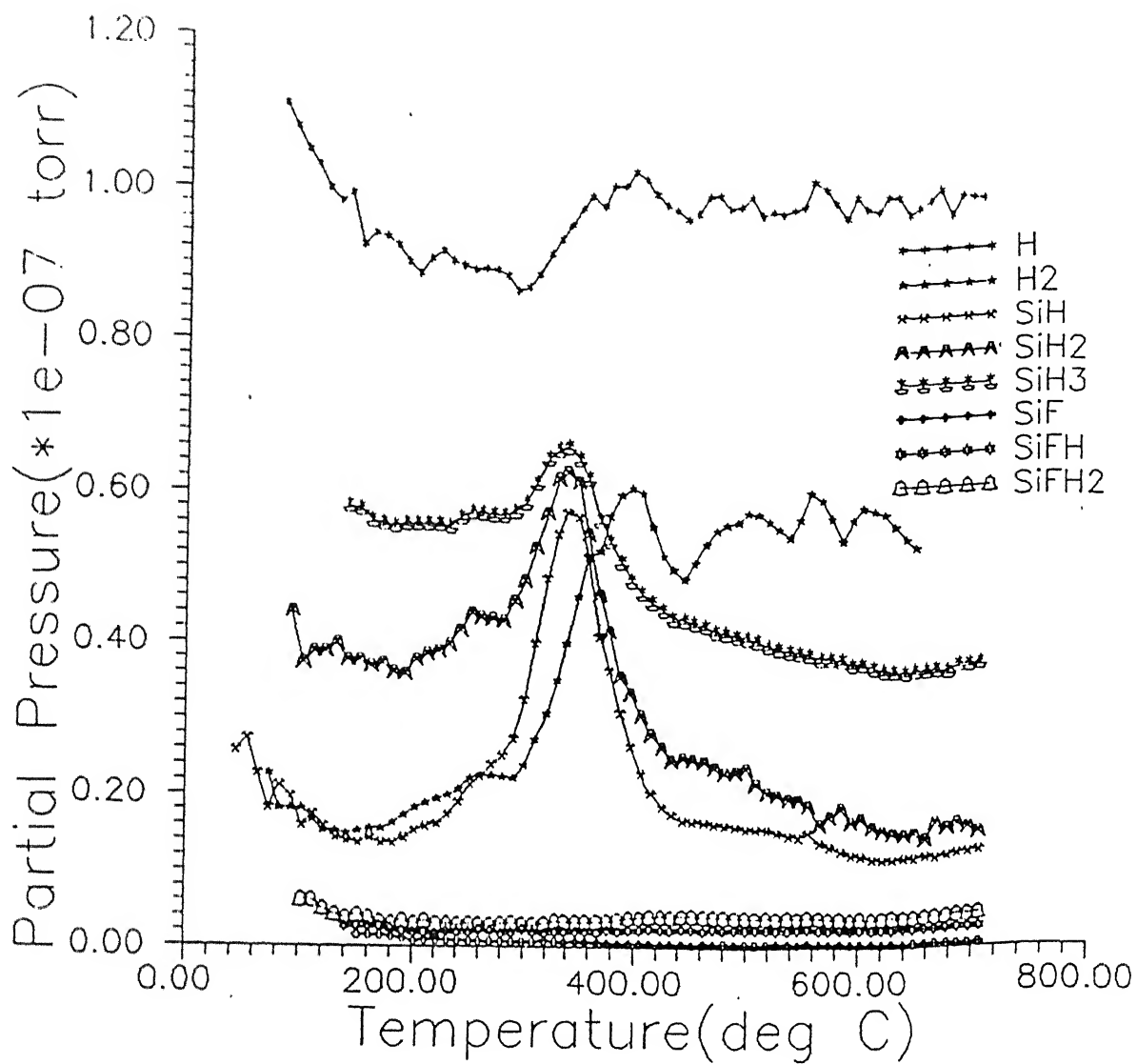


Fig.. 3.14 Thermal gas effusion spectrum of PSL11 as a function of temperature.

$m/e=2$  was assigned to the molecular hydrogen and not to  $He^{2+}$  as the latter is not expected to be present in any significant amount in porous silicon sample because of the use of HF solution for etching. Similarly,  $m/e=29, 30$  and  $31$  are attributed to  $SiH^+$ ,  $SiH_2^+$  and  $SiH_3^+$ , respectively. Higher  $m/e$  assigned to fluorides of silicon.

The individual spectrum was analyzed using a peakfit software package. Fig. 3.15 shows the case of molecular hydrogen evolution from PSL1. It contains two peaks centred around  $376^\circ$  and  $476^\circ\text{C}$  with FWHM of  $38.6^\circ$  and  $139.7^\circ\text{C}$ , respectively. Figs. 3.16 - 3.18 depict the spectra and their fitted curves for  $SiH$ ,  $SiH_2$  and  $SiH_3$  species. It is interesting to note that all of them have central maxima within  $330^\circ - 350^\circ\text{C}$ . These results suggest that  $SiH$  species are evolved nearly at the same temperature and presumably lie on the surface of the crystallites. The hydrogen trapped in pores and present interstitially in silicon crystallites gets released around  $376^\circ$  and  $476^\circ\text{C}$ .

Assuming that the kinetics of gas desorption processes follow a rate equation [57]

$$\frac{dN}{dt} = A(1 - N)^n \exp(-E_a/RT) \quad (3.1)$$

where  $N$  is the fraction of gas evolved by overcoming the free energy barrier  $E_a$ ,  $A$  is a pre-exponential factor,  $n$  is order of reaction and  $R$  is gas constant. If temperature rises at a constant heating rate, the evolution rate will first rise to a maximum value and then return to zero when the process of effusion ceases. The temperature ( $T_m$ ) corresponding to maximum evolution rate determines the stability or bonding strength of the evolving atom/molecule. The activation energy  $E_a$  for the case of constant heating rate can be shown to be related to  $T_m$  as

$$E_a = -2RT_m \quad (3.2)$$

The values of  $E_a$  estimated from  $T_m$  data are given in Table 3.5. Accordingly, activation energies for effusion of  $^{cell}_{\wedge}SiH_x$  are  $\sim 1.05$  eV and of hydrogen 1.12 and 1.28 eV.

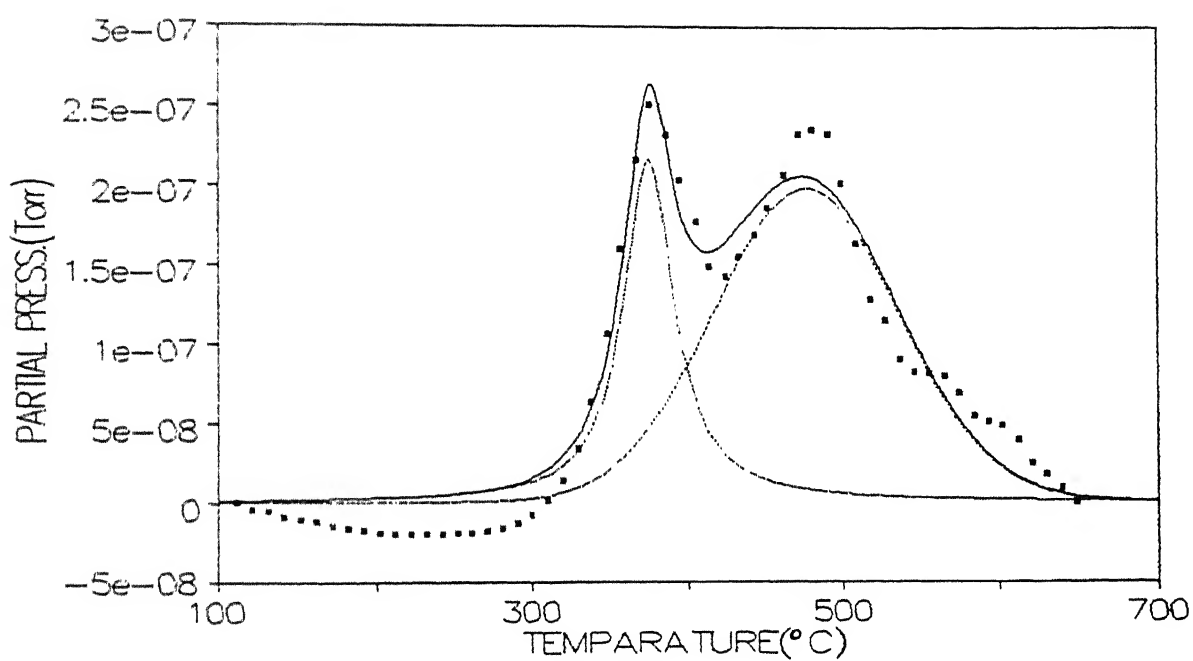


Fig 3.15 Hydrogen gas evolution characteristic of PSL1 as derived from "peak fit" analysis of experimental data.

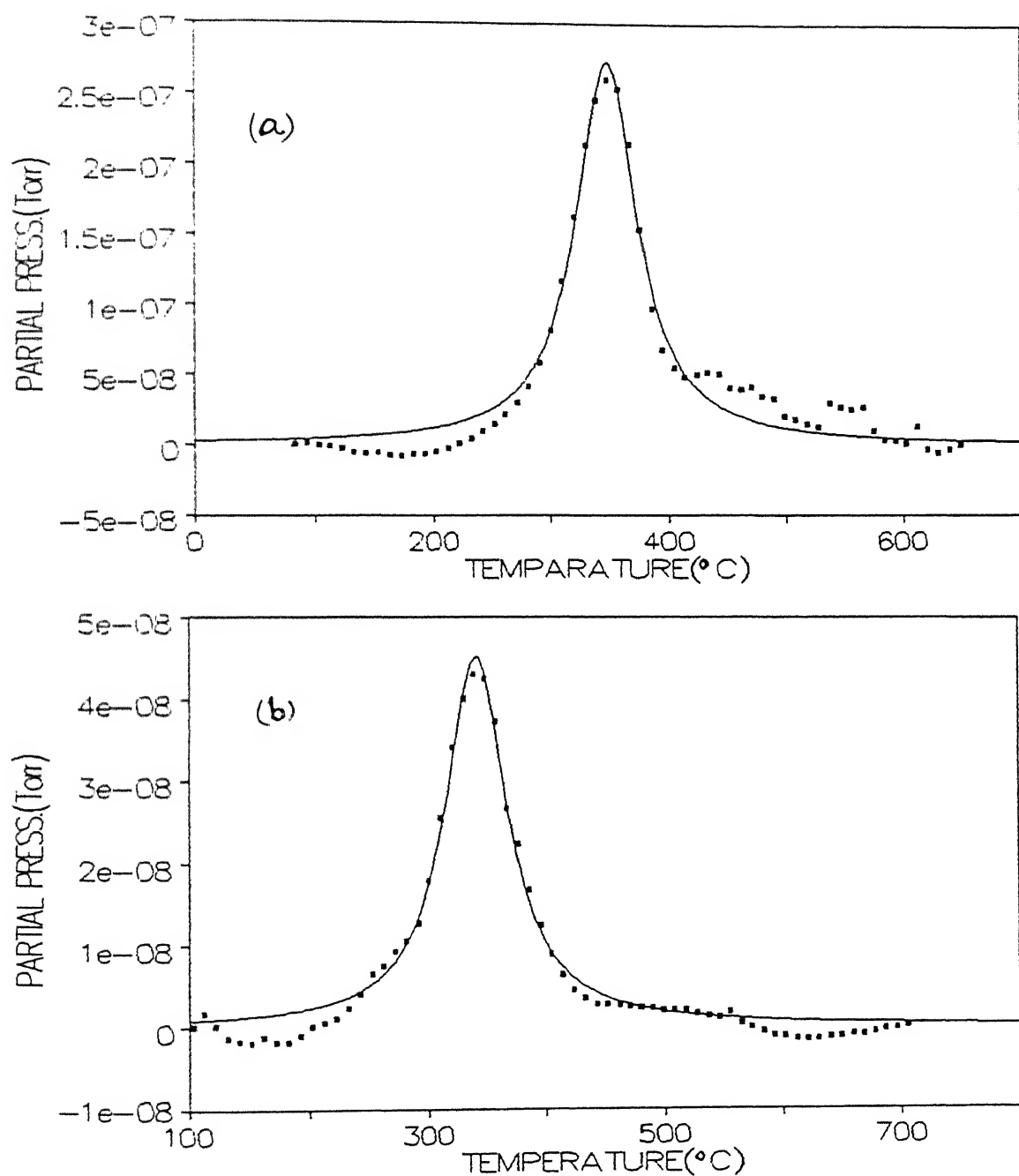


Fig. 3.16 SiH gas evolution characteristic of (a) PSL1 and (b) PSL11 as derived from "peak fit" analysis of experimental data.

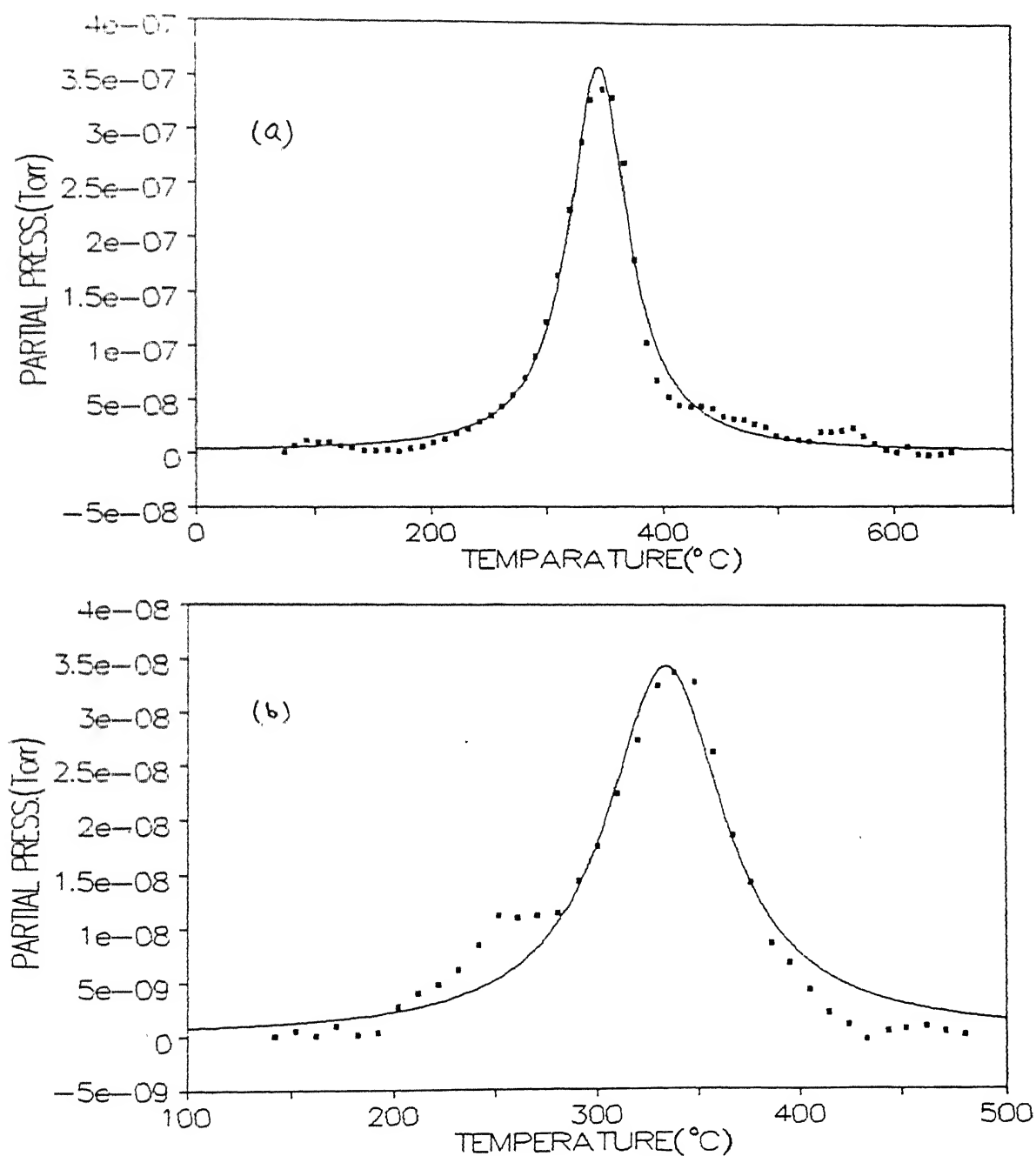


Fig. 3.17  $\text{SiH}_2$  gas evolution characteristic of (a) PSL1 and (b) PSL11 as derived from "peak fit" analysis of experimental data.

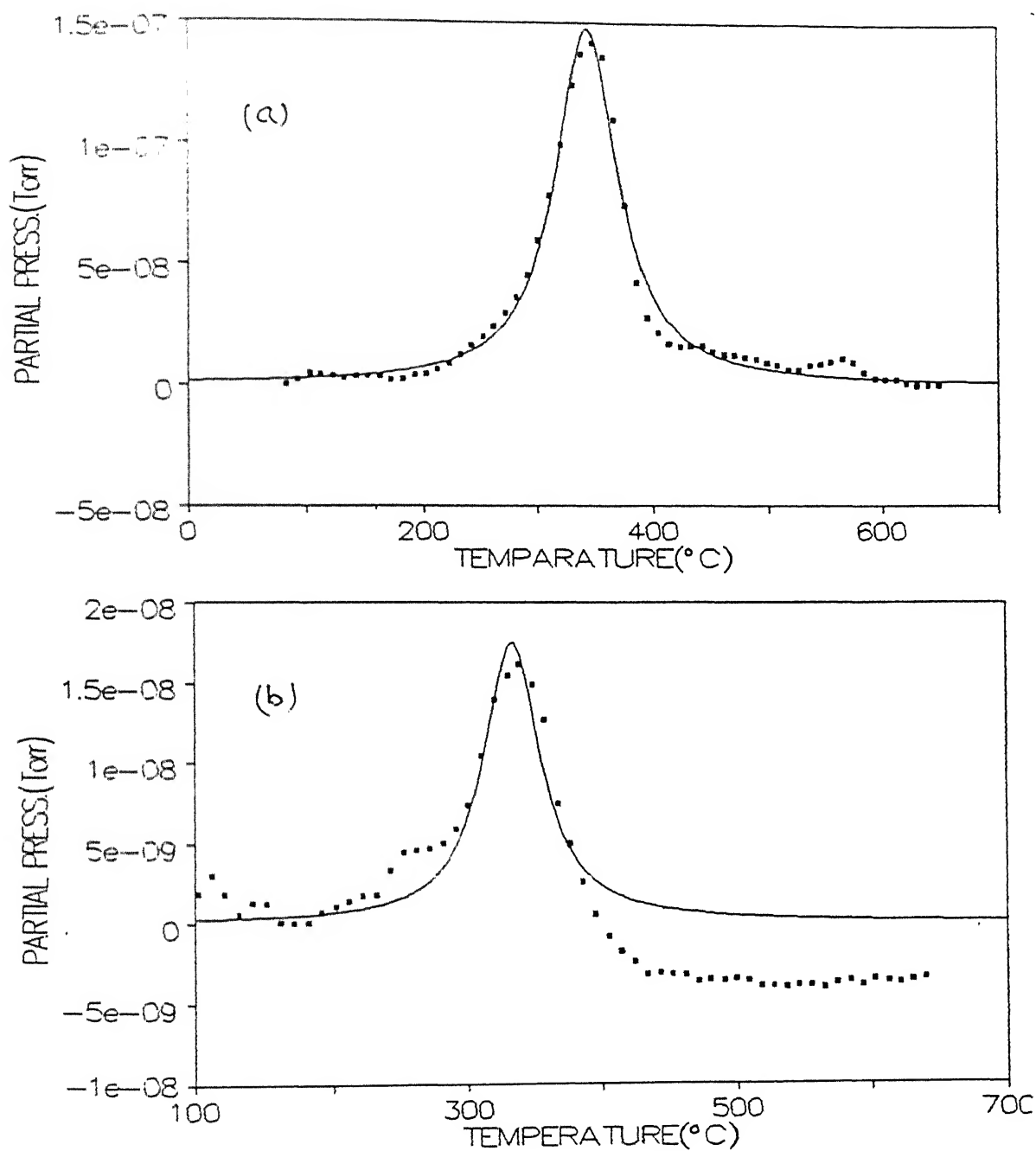


Fig. 3.18  $\text{SiH}_3$  gas evolution characteristic of (a) PSL1 and (b) PSL11 as derived from "peak fit" analysis of experimental data.



Table 3.5. Thermal gas effusion data of porous silicon in the process of annealing at the rate of  $9.6^{\circ}\text{C}/\text{min}$  under vacuum  $\sim 10^{-6}$  torr.

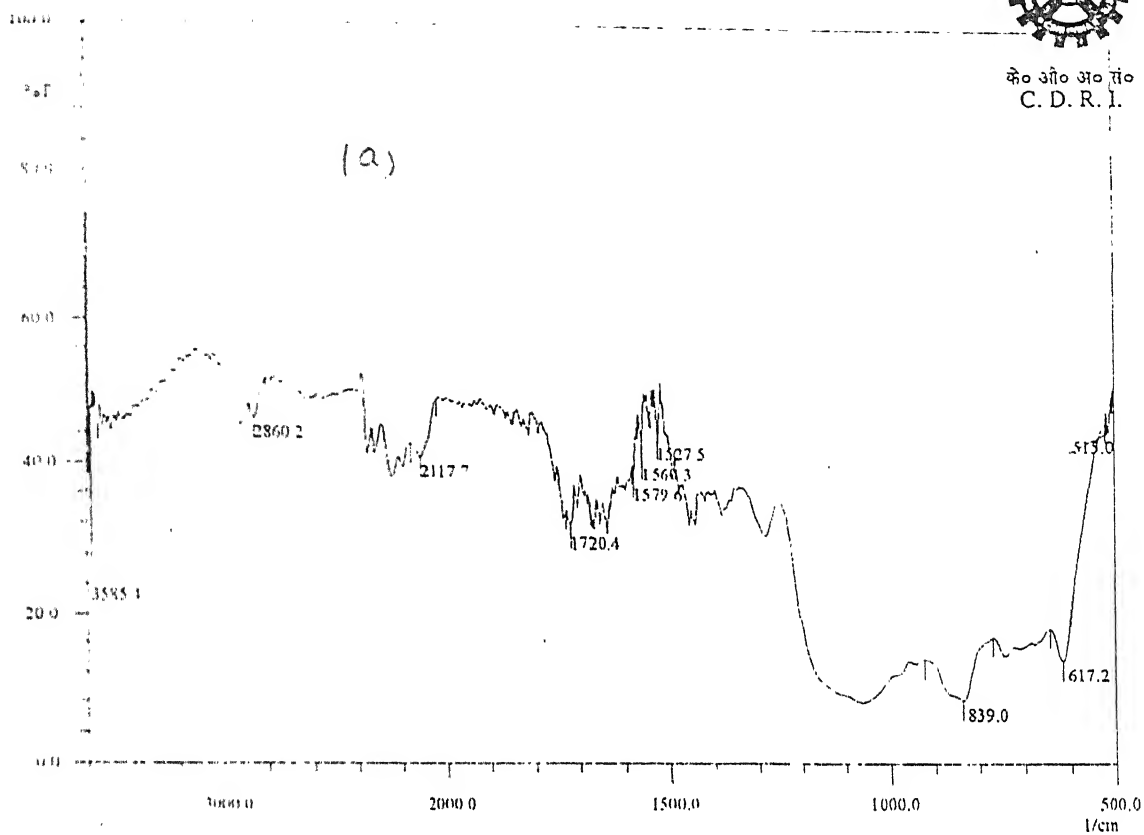
Sample	gas evolved	Temperature ( $T_m$ ) for maximum partial pressure or central maxima ( $^{\circ}\text{C}$ )	FWHM ( $^{\circ}\text{C}$ )	Area under peak $\times 10^5$ (Torr $^{\circ}\text{C}$ )	$E_a \simeq -2RT_m$ (eV)
PSL1	$\text{H}_2$	376, 476	38.6, 139.7	1.2, 2.9	1.11, 1.28
	$\text{SiH}$	348	62.8	2.5	1.06
	$\text{SiH}_2$	345	61.4	3.2	1.05
	$\text{SiH}_3$	343	66.1	1.4	1.05
PSL11	$\text{SiH}$	340	64.5	0.4	1.04
	$\text{SiH}_2$	334	70.4	0.3	1.04
	$\text{SiH}_3$	333	51.7	0.1	1.04

### 3.5 FTIR studies

The energies associated with the infrared region correspond to vibrational mode of atoms in solids. Consequently, IR spectroscopy can in principle analyze the nature of bonding of silicon atoms with hydrogen, oxygen, etc. Fig. 3.19 shows a typical FTIR spectra of PSL2 porous silicon in virgin state and after annealing upto  $450^{\circ}\text{C}$  in the wavenumber range of  $500\text{-}3600\text{ cm}^{-1}$ . Also, FTIR spectra for PSL6 (virgin and annealed upto  $250^{\circ}\text{C}$ ) and PSL13 (virgin) samples are presented in Figs 3.20 and 3.21, respectively. Table 3.6 summarizes the infrared absorption data available in the literature for vibrational modes and species relevant to porous silicon [59-67]. The present FTIR data when examined carefully, it was noticed that while some peaks match well with the known modes (stretching or deformation)/species, others found for the first time in virgin/annealed samples of porous silicon. The wavenumbers of peak positions, percentage absorption at peak maxima and their possible origin are listed in Tables 3.7, 3.8 and 3.9 for PSL2, PSL6 and PSL13 samples, respectively. Also, after annealing of samples upto  $250^{\circ}\text{C}$  or  $450^{\circ}\text{C}$ , a



के० औ० अ० सं०  
C. D. R. I.



के० औ० अ० सं०  
C. D. R. I.

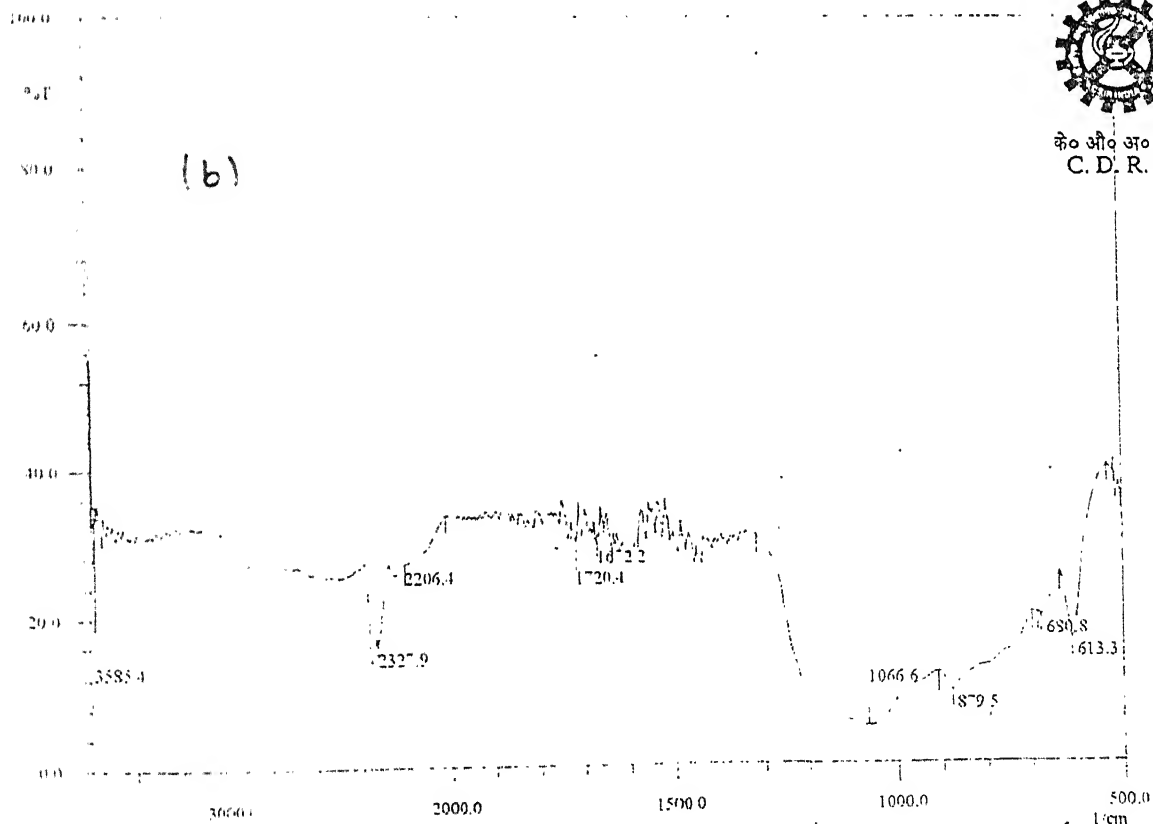
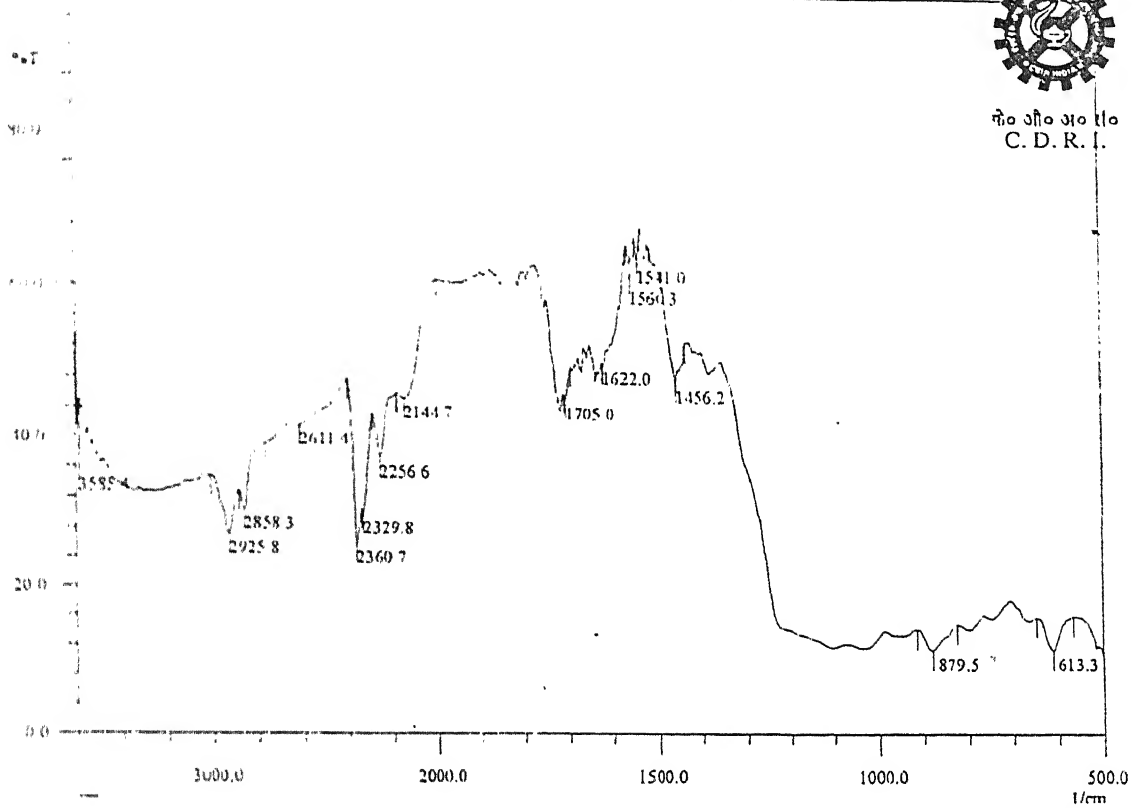


Fig. 3.19 FTIR spectra of PSL2 (a) in virgin state and (b) after annealing upto  $450^{\circ}\text{C}$ .



के. डी. आर. सं.  
C. D. R. I.



के. डी. आर. सं.  
C. D. R. I.

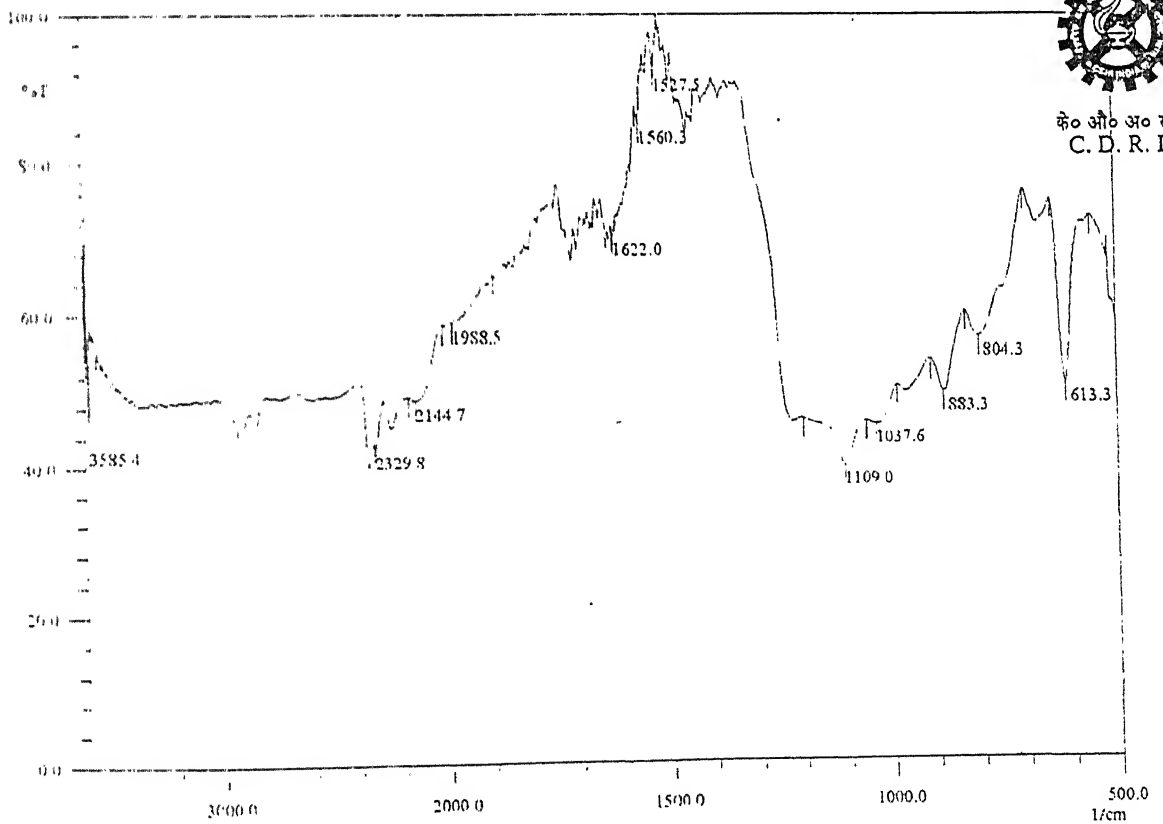


Fig. 3.20 FTIR spectra of PSL6 (a) in virgin state and (b) after annealing upto 250°C.



के० आर० आर०  
C. D. R. I.

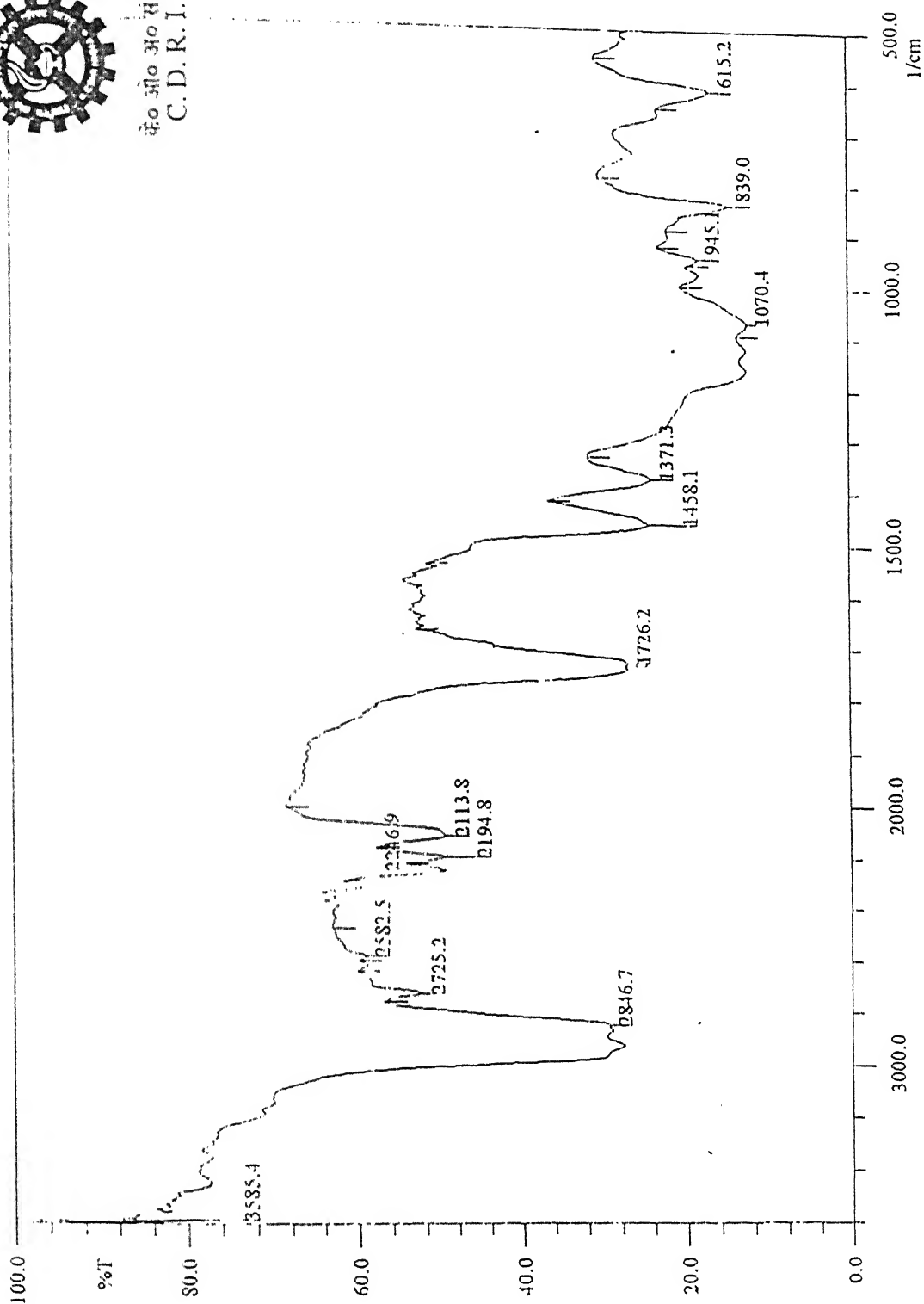


Fig 3.21 FTIR spectra of PSL13 in virgin state.

Table 3.6 Summary of the IR data available in the literature for vibrational modes and species relevant to porous silicon [56-67]

S No	Mode species	Characteristic peak maxima on band range wavenumber ( $\text{cm}^{-1}$ )	Remark (s)
1	Silicon longitudinal optical and transverse acoustical mode	814, 742, 628 (611 - 617)*	Si-Si stretching * in uncorrected IR data
2	Si-H stretching modes of $\text{H}_2$ bonded hydroxyls bending mode	3000-3800 800-900	broad and composite absorption broad and weak
3	Hydride species $\text{SiH}_x$ groups linked to Si stretching mode  deformation mode	2111 (SiH) 2089 (SiH <sub>2</sub> ) 2140 (SiH <sub>3</sub> ) 628 (SiH)  665-668 (SiH <sub>2</sub> ) 906-916 (SiH <sub>2</sub> ) 862	Wag (significant contribution) Wag scissor strong
4	Si-O-Si bonds formed with interstitial oxygen. Oxygen substitution into background of SiH stretching	1000-1200 (or 1106) 2143 2240	Asymmetric stretching broad; vibrations (appears after ageing)
5	$\text{SiH}_x$ groups linked with oxygen: stretching mode deformation modes	2200 ( $\text{O}_2$ -SiH <sub>2</sub> species) 2258 ( $\text{O}_3$ -SiH species) 750 814 850 $\text{O}_y$ -Si-H <sub>x</sub> 878 940	blue shift in PL contribution due to Si-O-H bending mode, O-Si-O symmetrical stretching mode also fall in this region
6	$\text{SiO}_2$ islands asymmetrical stretching vibrations of bulk O-Si-O bridge HO-Si-H group on silica surface highly distorted siloxene bridges on silica	1106 1200 (shoulder)  2240 2147  1061 1153 812-814 850 (Shoulder)	Shift occurs to 1061 and 1153 (shoulder) with ageing  SiH stretching mode include contribution from surface hydroxyls, $\text{O}_y\text{SiH}_x$ species and O-Si-O symmetrical stretching mode of $\text{SiO}_2$ layer
7	Carbonate species	1707-1720 1288-1304	Stretching modes

Table 3.7 FTIR spectrum data of PSL2 giving of peak position, percentage absorption at peak maxima and corresponding modes/species.

Virgin sample		After annealing upto 450 <sup>0</sup> C		Assignment of modes/species
Peak position wavenumber (cm <sup>-1</sup> )	% Absorption at peak maxima	Peak position wavenumber (cm <sup>-1</sup> )	% Absorption at peak maxima	
617	86	613	84	Si-Si stretching SiO-H bending mode/highly disordered siloxene bridge on
839	92	-	-	
-	-	879	90	deformation mode O <sub>γ</sub> -Si-H <sub>2</sub> species
Broad peak 1060	-	1066	95	Si-O-Si asymmetric stretching vibration
1527	57	-	-	New peaks; disappear after annealing
1560	57	-	-	
-	-	1672	70	appears after annealing
1720	69	1720	70	Carbonate species stretching mode
2117	59	-	-	SiH wagging
-	-	2206	73	SiH <sub>x</sub> groups linked with oxygen; O <sub>2</sub> -Si-H <sub>2</sub> , O <sub>3</sub> -Si-H species in stretching mode
-	-	2254	17	
-	-	2327	84	
2860	54	-	-	New peak (disappears after annealing)
3585	75	3585	85	SiO-H stretching modes of hydrogen bonded hydroxyls

Table 3.8: FTIR spectrum data of PSL6 giving of peak position, percentage absorption at peak maxima and corresponding modes/species.

Virgin sample		After annealing upto 250°C		Assignment of modes/species
Peak position wavenumber (cm <sup>-1</sup> )	% Absorption at peak maxima	Peak position wavenumber (cm <sup>-1</sup> )	% Absorption at peak maxima	
613	89	613	50	Si-Si stretching deformation mode O <sub>y</sub> -Si-H <sub>x</sub> species; SiO-H bending mode
879	89	883	50	
Broad peak	-	1037	55	Si-O-Si asymmetric stretching vibration
1541	37	1527	8	New peaks % absorption decreases after annealing
1560	37	1560	15	
1622	50	1622	30	
1705	55	-	-	Carbonate species stretching mode
2144	55	2144	51	SiH <sub>3</sub> wagging; SiH stretching mode
2256	63	-	-	Oxygen related peaks O <sub>3</sub> -Si-H species
2330	70	2330	58	New peak; height decreases on annealing upto 250°C
2858	70	-	-	New peak; height disappears on annealing
3585	65	3585	57	SiO-H stretching modes of hydrogen bonded hydroxyls

Table 3.9: FTIR spectrum data of PSL13 giving of peak position, percentage absorption at peak maxima and corresponding modes/species.

Virgin sample		Assignment of modes/species
Peak position wavenumber (cm <sup>-1</sup> )	% Absorption at peak maxima	
615	83	Si-Si stretching
839	85	deformation mode O <sub>y</sub> -Si-H <sub>x</sub> species; SiO-H bending mode
945	82	SiO-H bending mode/SiH <sub>2</sub> scissor
1070	82	Si-O-Si asymmetric stretching vibration
1458	76	New peak
1726	73	Carbonate species stretching mode
2114	50	SiH wagging
2195	50	O <sub>2</sub> -Si-H <sub>2</sub> stretching mode
2247	50	O <sub>3</sub> -Si-H stretching mode
2847	70	New peak
3585	25	SiO-H stretching modes of hydrogen bonded hydroxyls



and some new show up. The peaks which disappear correspond to  $\text{SiH}_x$  species or SiO-H bending mode. Such a result is consistent with the thermal gas effusion findings discussed in the previous section, viz., evolution of hydrogen,  $\text{SiH}_x$ , etc. Also, annealing is likely to cause oxidation and therefore new peaks at 2254 and 2327  $\text{cm}^{-1}$  corresponding to stretching mode of  $\text{O}_2\text{-Si-H}_2$  and  $\text{O}_3\text{-Si-H}$  species result in PSL2. It is interesting to note that such peaks are seen even in as prepared (i.e. virgin) PSL6. The reason for this perhaps lies in the longer etching time used for PSL6 and/or the peaks belong to some other modes/species.

In summary, porous silicon is an inhomogeneous material consisting of the pores and silicon skeleton with nanostructures. Also, there lies a number of species on surface and/or in pore regions, viz.,  $\text{SiH}_x$ , hydrogen, hydroxyls, oxygen related species, carbonates,  $\text{SiO}_2$ , etc. On annealing, hydrogen and its related species evolve and emergence of oxygen associated species occurs. Also, the photoluminescence (PL) is found to decrease with annealing. This means that non-radiative recombination centres are enhanced on the surface, as evident from EPR studies (see, e.g., section 3.3). The origin of PL in porous silicon lies with the radiative recombination centres associated with the species present on surface or in pore regions besides quantum confinement effects (i.e., band gap enhancement) in nanostructures of silicon. Since, PS exhibits high porosity ( $\sim 70\text{-}80\%$ ) and, in turn, specific surface area of several hundreds  $\text{m}^2$  per gram [68], the contribution to PL from these regions is expected to be quite significant. This inference derives support even from the X-ray diffraction studies (see, e.g., section 3.2) which continue to reveal the presence of nanosized silicon crystallites in annealed porous silicon samples.

### Conclusions

- (1) Photoluminescence grade porous silicon has been prepared by electrochemical etching of p-type silicon wafers (resistivity 0.3-1.5  $\Omega$ -cm, <100> orientation) in 1:1 mixture of 48% HF and C<sub>2</sub>H<sub>5</sub>OH at a current density of 5-10 mA/cm<sup>2</sup> for 15-120 minutes.
- (2) Raman spectra of porous silicon contains three peaks centred around 519-521 cm<sup>-1</sup>, 502-513 cm<sup>-1</sup> and 473-490 cm<sup>-1</sup> (weak and broad) originating from c-Si, nanocrystallites (< 5 nm) and a-Si, respectively. Further, asymmetry nature of Raman spectrum towards lower wavenumbers suggest the existence of nanosized silicon crystallites/strain in PS. Annealing of PS makes the Raman spectrum progressively symmetrical as the crystallites grow in size and/or strains gradually disappear in the process.
- (3) The crystallites present in PS are of diamond-type silicon (lattice parameter  $a = 5.4307 \text{ \AA}$ ), have nanometer size (< 5 nm) and maintain the orientation [100] of the original silicon wafer. Annealing of PS at 250-650°C leads to increase in crystallite size by ~ 25-50% and causes gas effusion.
- (4) EPR signal with g-value 2.0061-2.0067 results due to trigonally symmetric silicon dangling bonds along <111> direction. The enhancement of EPR signal in PS upon annealing can be attributed to (i) increase in the number of dangling bonds passivated by hydrogen or other species earlier and (ii) many fold increase of the corresponding spin density. The defects associated with the dangling bond are non-radiative type as PL decrease sharply with rise in the spin density.
- (5) Porous silicon effuses molecular hydrogen, oxygen, SiH<sub>x</sub> and fluoride species on annealing in vacuum. Hydrogen trapped in pores and present interstitially in silicon gets evolved around 376°C and 476°C whereas, SiH, SiH<sub>2</sub> and SiH<sub>3</sub> species effuse at ~330-350°C; their activation energies being 1.11, 1.28 eV for hydrogen and 1.05 eV for SiH<sub>x</sub> species.

(6) The absorption peaks in FTIR spectrum of porous silicon either match very well with the known vibration modes/species, such as Si-Si stretching ( $\sim 613\text{-}617\text{ cm}^{-1}$ ), SiO-H stretching or bending/highly disordered siloxene bridge ( $\sim 839$  and  $3585\text{ cm}^{-1}$ ), Si-O-Si asymmetric stretching ( $\sim 1060\text{-}1070\text{ cm}^{-1}$ ), carbonate species stretching mode ( $1720\text{-}1726\text{ cm}^{-1}$ ), SiH<sub>x</sub> grouping ( $2110\text{-}2150\text{ cm}^{-1}$ ), or appear for the first time (e.g., at 1458, 1527, 1570, 2330,  $2840\text{-}2860\text{ cm}^{-1}$ ). After annealing, peaks corresponding to SiH<sub>x</sub> species or SiO-H bending mode disappear altogether, while new ones appear at 2254 and  $2327\text{ cm}^{-1}$  and correspond to stretching modes of O<sub>2</sub>-Si-H<sub>2</sub> and O<sub>3</sub>-Si-H species respectively.

## References

1. R. T. Collins, P. M. Fanchet and M. A. Tischler, *Physics Today*, January 24, (1997).
2. L. T. Canham, *Appl. Phys. Lett.*, **57**, 1046 (1990).
3. A. Uhler, *Bell system Tech J.* **35**, 333 (1956).
4. R. E. Hummel and S. S. Chang, *Appl. Phys. Lett.*, **61**, 1965 (1992).
5. D. Ruter, T. Kunze, and W. Bauhofer, *Appl. Phys. Lett.*, **64**, 3006 (1994).
6. K. W. Cheah and C. H. Choy, *Solid State Commun.*, **91**, 795 (1994).
7. N. Noguchi and I. Suemune, *Appl. Phys. Lett.*, **62**, 1429 (1993).
8. S. Banerjee, *Bull. Mater. Sci.*, **17**, 533 (1994).
9. Y. Kanemitsu, *Phys. Rev. B*, **48**, 12357 (1993).
10. J. R. Haynes and W. C. Westphal, *Phys. Rev.*, **101**, 1676 (1956).
11. W. Michaels and M. H. Pilkuhn, *Physica Status Solidi*, **36**, 311 (1969).
12. G. D. Francia, P. Maddalena, and D. Ninno, *Solid State Commun.*, **96**, 579 (1995).
13. H. Koyama, Minoru Araki, Yuko Yamamoto, and Nobuyoshi Koshida, *Jpn. J. Appl. Phys.*, **30**, 36006 (1990).
14. Joginder Singh, AC and DC transport in electrochemically etched porous silicon layers M. Tech Thesis, IIT Kanpur, (1996).
15. M. I. J. Beale, J. Benjamin, M. J. Uren, N. G. Chew, and A. G. Cullis, *J. Cryst. Growth*, **73**, 622 (1985).
16. M. S. Brandt, H. D. Fuchs, M. Strutzmann, J. Weber, and M. Cardona, *Solid State Commun.*, **81**, 307 (1992).
17. A. G. Cullis and L. T. Canham, *Nature*, **353**, 335 (1991).
18. D. J. Dimaria, J. R. Kirtley, E. J. Pakulis, D. W. Dong, T. S. Kuan, F. L. Pesavento, T. N. Thus, J. A. Kutro, and S. D. Brorson, *J. Appl. Phys.*, **56**, 4011 (1984).
19. S. Furukawa and T. Miyasato, *Phys. Rev. B*, **38**, 5726 (1988).
20. H. Foll, *Appl. Phys. A* **53**, 8, (1991).
21. H. Takagi, H. Ogawa, Y. Yamazaki, A. Ishizaki, and T. Nakagiri, *Appl. Phys. Lett.*, **56**, 2379 (1990).
22. F. Kozlowski, V. Petrova Koch, A. Kux, W. Stadler, A. Fleischmann, and H. Sigmund, *J. Non-Cryst. Solids*, **137/138**, 91 (1991).

23. S. M. Prokes, O. J. Glembocki, V. M. Bermudez, R. Kaplan, L. E. Friedersdorf, and P. C. Searson, *Phys. Rev. B*, **45**, 13788 (1992).
24. C. Tsai, K. H. Li, D. S. Kinosky, R. Z. Qian, T. C. Hsu, J. T. Irby, S. K. Banerjee, A. F. Tasch, J. C. Campbell, B. K. Hance, and J. M. White, *Appl. Phys. Lett.*, **60**, 1700 (1992).
25. A. Halimaoui, C. Oules, G. Bomchil, A. Bsiesy, F. Gaspard, R. Herino, M. Ligen, and F. Muller, *Appl. Phys. Lett.*, **59**, 304 (1991).
26. N. Koshida and H. Koyama, *Appl. Phys. Lett.*, **60**, 347 (1992).
27. P. Steiner, F. Kozlowski, and W. Lang, *Appl. Phys. Lett.*, **62**, 2700 (1993).
28. J. C. Mao, Y. Q. Jia, J. S. Fu, E. Wu, B. R. Zhang, L. Z. Zhang, and G. G. Qin, *Appl. Phys. Lett.*, **62**, 12 (1993).
29. M. A. Butturi, M. C. Carotto, G. Martinelli, L. Passari, G. M. Youesef, A. Chirino, and G. Ghotti, *Solid State Commun.* **101**, 11 (1997).
30. Z. Iqbal, S. Veprek, A. P. Webb, and P. Capezzuto, *Solid State Commun.* **37**, 993 (1981).
31. A. Roy, K. Jayaram and A. K. Sood, *Solid State Commun.* **89**, 229 (1994).
32. J. Singh, Thermal effusion studies on porous silicon, M.Tech thesis, I.I.T. Kanpur, 1997.
33. M. B. Robinson, A. C. Dillon, D. R. Haynes, and S. M. George, *Appl. Phys. Lett.*, **61**, 1414 (1992).
34. George C. John and V. A. Singh, *Physics Reports*, **263**, 93 (1995).
35. T. Nakayama, K. Yakubo, and R. L. Orbach, *Rev. Mod. Phys.*, **66**, 381 (1994).
36. Y. Gefen, A. Aharony, and S. Alexander, *Phys. Rev. Lett.*, **50**, 77 (1983).
37. R. L. Smith, and S. D. Collins, *J. Appl. Phys.*, **7**, R1 (1992).
38. B. D. Cullity, *Elements of X-ray Diffraction*, 2nd edition, Addison-Wesley, Reading Massachusetts, (1978), p.99.
39. R. Tsu, H. Shen, and M. Dutta, *Appl. Phys. Lett.*, **60**, 112 (1992).
40. I. Gregora, D. Champagnon, and A. Halimaoui, *J. Appl. Phys.* **75**, 3034 (1994).
41. L. Pavesi, M. Anderi and L. Fedrizzi, *J. Appl. Phys.* **75**, 1118 (1994).
42. A. Roy, K. Jayaram, and A. K. Sood, *Bull. Mater. Sci.*, **17**, 513 (1994).
43. H. Richter, Z. P. Wang, and L. Ley, *Solid State Commun.* **39**, 625 (1986).
44. I. H. Campbell and P. M. Fauchet, *Solid State Commun.* **58**, 739 (1986).

45. M. Yang, D. Huang and P. Hao, Appl. Phys. Lett., **75**, 651 (1994).
46. A. Roy, K. Jayaram, and A. K. Sood, Bull. Mater. Sci. **17**, (5), 513 (1994).
47. M. A. Stathis, R. T. Collins, J. H. Stathis and J. C. Tsang, Appl. Phys. Lett., **60**, 639 (1992).
48. S. V. Bhat, K. Jayaram, D. Victor, S. Muthu and A. K. Sood, Appl. Phys. Lett., **60**, 2116 (1992).
49. J. C. Mao, Y. Q. Jia, J. S. Fu, E. Wu, B. R. Zhang, L. Z. Zhang and G. G. Qin, Appl. Phys. Lett., **62**, 12 (1993).
50. G. D. Watkins and J. W. Corbett, Phys. Rev. **134**, A 1359 (1964).
51. M. Nisenoff and H. Y. Fan, Phys. Rev. **128**, 1605 (1962).
52. K. L. Brower, Phys. Rev. Lett. **44**, 1627 (1980).
53. A. Stesmans, Appl. Phys. Lett., **48**, 972 (1986).
54. P. J. Caplan, E. H. Poindexter, B. E. Deal and R. R. Razauk, J. Appl. Phys. **50**, 5847 (1979).
55. H. Ubaro, T. Imura, A. Wiraki, I. Hirabayashi and K. Morigaki, J. Non. Cryst. solid **59** and **60**, 641 (1983).
56. Alok Srivastava and S. C. Agarwal Symp. Proc. *National Symposium on Physics of Semiconductor nanostructurs*, New Delhi (1997) p.155.
57. W. Beyer and H. Wagner, J. Appl. Phys., **53**, (12) 8745 (1982).
58. M. S. Brandt, H. D. Fuchs, M. Stutzmam, and M. Cardone, Solid State Commun. **81**, 307 (1992).
59. J. M. Lavine, S. P. Sawan, T. Sheieh, and A. J. Bellizza, Appl. Phys. Lett., **62**, 1099 (1993).
60. C. Tsai, K. H. Li, D. S. Kinosky, R. Z. Qian, T. C. Hsu, J. T. Irhy, S. K. Banerjee, A. F. Jasch, J. C. Compbell, B. K. Hance, and J. M. White, Appl. Phys. Lett., **60**, 1700 (1992).
61. S. Lin, C. Palsule, S. Yi and S. Gangopadhyay, Physical Review B, **49**, 10318 (1994).
62. M. A. Butturi, M. C. Carotta, G. Martineli, L. Passari, G. M. Youssef, A. Chiorino and G. Ghiotti, Solid State Commun., **101**, (11-16) (1997).
63. C. Morterra, M. J. D. Lew, J. Phys. Chem. **73**, 327 (1969).
64. P. Gupta, A. C. Dellon, A. S. Bracker and S. M. George, Surf. Sci. **245**, 360 (1991).

- 65 M Hory et. al., Thin Solid Films **255**, 200 (1995).
- 66 Y Ogata, H. Niki, T. Sakka and M. J. Iwasaki, Electrochem. Soc. **142**, 1595 (1995).
- 67 H C. Verma, George C. John, and Vijay A. Singh Physical Review B **53** (15) 53 (1996).
- 68 A Halimaoui, in "Optical properties of low-dimension silicon structures", D. C. Bensahel, L. T. Canham and S. Ossicini (eds.), NATO ASI series E: Applied Sciences, Kluwer Academic Publishers, Dordrecht, Boston, (1993), p.11.

124452

## Date Slip

This book is to be returned on the  
date last stamped **124452**

124452

MSP-1897-NI-GIN-876



A124452